thesis for the degree of doctor of philosophy in Thermo and Fluid Dynamics

---

Ballistic and Optical Imaging of Transient Fuel Sprays for Dual-Fuel Combustion

Transient Spray Mode Fuel Injection

Lokesh Mopuri

Division of Transport, Energy and Environment
Department of Mechanics and Maritime Sciences
Chalmers University of Technology
Göteborg, Sweden, 2025

Ballistic and Optical Imaging of Transient Fuel Sprays for Dual-Fuel Combustion

Transient Spray Mode Fuel Injection

Lokesh Mopuri

Doktorsavhandlingar vid Chalmers tekniska högskola
Ny serie nr. 5775
ISSN 0346-718X
ISBN 978-91-8103-318-2
DOI https://doi.org/10.63959/chalmers.dt/5775
Division of Transport, Energy and Environment
Department of Mechanics and Maritime Sciences
Chalmers University of Technology
SE-412 96 Göteborg, Sweden
Phone: +46 (0)31 772 1000
`https://www.chalmers.se`

Printed by Chalmers Reproservice
Göteborg, Sweden, 2025

To my esteemed mentors, ***Prof. David Sedarsky*** *and* ***Dr. Jari Hyvönen***

Abstract

Pilot sprays play a vital role in dual-fuel (DF) combustion applications, where a small quantity of liquid fuel is used to ignite the primary gaseous fuel. The quantity and distribution of the pilot spray have a significant influence on combustion efficiency and the formation of harmful exhaust emissions. This study examines the fuel spray characteristics of heavy-duty marine diesel injectors using optical diagnostics. In dual-fuel operation, these injectors operate in a transient mode due to shortened dwell times and limited needle lifts, which directly impact the spray breakup and atomization processes. The objective is to investigate the behavior of transient sprays under high-pressure and high-temperature ambient conditions. Experiments were conducted in optically accessible spray test rigs that replicate in-cylinder environments. Initially, multi-hole (MH) injectors were investigated using the Mie-scattering technique to analyze plume-to-plume variations under non-evaporative and non-reactive conditions. Afterward, the focus shifted to studies of single-spray plumes; to achieve this, the thimble method was implemented. A thimble is a small metal cap placed on the nozzle tip that isolates a single spray plume from a multi-plume spray, while collecting the remaining plumes and directing them into a drain passage. This method enables the study of individual spray characteristics without interference from adjacent plumes and without altering the nozzle geometry. Single spray experiments were carried out under various conditions, including non-evaporative and non-reactive sprays, evaporative and non-reactive sprays, and reactive sprays. A diffuse back-illumination (DBI) technique was used to visualize the liquid phase, while Schlieren imaging captured evaporative and reactive sprays. Natural luminosity imaging was used to capture both the low-temperature combustion (LTC, or cool-flame) and high-temperature combustion (HTC) regimes in the reacting spray. The low-temperature combustion (LTC) or cool-flame phase, observed at approximately 850 K ($\pm$50 K), appeared as a blue flame, indicating gas-phase oxidation with negligible soot formation due to lower flame temperatures and relatively uniform fuel–air mixing. In contrast, the high-temperature combustion (HTC) phase, observed at around 1150 K ($\pm$50 K), exhibited a yellow flame resulting from higher local temperatures, locally fuel-rich regions, and notable soot formation, whose thermal radiation dominated the luminosity signal under these conditions. Lastly, near-field atomization behavior was investigated using time-resolved ballistic imaging (BI), which captures spray evolution and breakup phenomena within 10 mm of the nozzle exit. These experiments (BI) were conducted under ambient back-pressure conditions only, with fuel injection pressures systematically varied from 1700 to 2100 bar to study their influence on spray development. Throughout all experiments conducted in this research, the ambient density was varied up to approximately 28 kg/m^3, and the injection pressure was varied up to 2100 bar. The results emphasize the combined influence of ambient density, fuel injection pressure, and temperature on the transient development of the spray.

Keywords: Spray characteristics, thimble structure, isolated spray, non-reactive sprays, evaporative sprays, reactive sprays, near-field atomization, Mie-scattering, diffuse back-illumination (DBI), Schlieren imaging, natural luminosity, ballistic imaging (BI)

List of Publications

This thesis is based on the following publications:

[A] **Mopuri, L.**, Grahn, V., Sedarsky, D., Hyvönen J., "Shape/penetration analysis and comparisons of isolated spray plumes in a multi-hole Diesel spray". Experiments in Fluids. 2024 Jun;65(6):92. https://doi.org/10.1007/s00348-024-03829-6.

[B] **Mopuri, L.**, Grahn, V., Sedarsky, D., Hyvönen J., "Impact of injector variability on transient spray characteristics in Diesel injectors". Atomization and Sprays. 35(9):1–21 (2025). https://doi.org/10.1615/AtomizSpr.2025058494.

[C] **Mopuri, L.**, Grahn, V., Sedarsky, D., Hyvönen J., "A Transient mode pilot sprays for dual-fuel combustion". Submitted ***(under review)***.

[D] **Mopuri, L.**, Grahn, V., Sedarsky, D., Hyvönen J., "Influence of ambient pressure, temperature, and injection pressure on reactive pilot n-heptane spray evolution using optical imaging". Submitted ***(under review)***.

[E] **Mopuri, L.**, Grahn, V., Sedarsky, D., Hyvönen J., "Time-resolved ballistic imaging of transient Diesel spray". Submitted ***(under review)***.

Acknowledgments

I would like to express my heartfelt gratitude to my mentors, **Prof. David Sedarsky** and **Dr. Jari Hyvönen**, for their invaluable guidance, profound expertise, and unwavering support throughout the course of this research. Their insightful feedback, clear direction, and generous investment of time enabled me to explore a subject of deep personal interest, and their mentorship was instrumental in the successful completion of this work.

I am also deeply thankful to **Prof. Mats Andersson** for his constructive suggestions and detailed feedback at multiple stages of my doctoral journey. His input significantly enhanced both the quality and focus of this study. I sincerely acknowledge Wärtsilä Finland Oy and the Combustion Engine Research Center (CERC) for providing the essential support, facilities, and resources required to carry out the experimental work. I am especially grateful to **Mohammad Nikouei** and **Viljam Grahn** for their assistance during various phases of the experiments. Their technical support and collaboration were truly appreciated. In addition, I would like to thank the professors, research engineers, and fellow researchers at the Division of Transport, Energy and Environment, Chalmers University of Technology, as well as at Wärtsilä, for their collaboration, support, and enriching discussions, which greatly contributed to the depth and progress of this work. I also extend my sincere gratitude to **Prof. Anand T. N. C.**, my Master's supervisor at **IIT Madras** (now at IIT Palakkad), for his belief in me, guidance, motivation, and support at various stages of my academic journey, which inspired me to develop a deeper interest in research, particularly in the field of optical diagnostics.

My sincere thanks also go to my dear friends, **Guravaiah Punugupati**, **Bosu Mandadapu, and Ekambaram Mopuri** for their constant encouragement, moral support, and genuine concern for my well-being. Their companionship and motivation during both challenging and memorable times have played a vital role in my personal and academic journey. I am truly grateful for their enduring friendship and invaluable presence in my life. I would also like to thank my friends, **Vajrala Srikanth Reddy** and **Vamsi Rapolu**, for the enjoyable moments, shared memories, and the joy we experienced together in Göteborg.

Finally, I express my deepest gratitude to my mother, **Thulasamma Mopuri**, and to the cherished memory of my late father, **Sreeramulu Mopuri**, for their unconditional love, encouragement, and sacrifices. I am also sincerely thankful to my brother, who is also a dear friend, **Ashok Kumar Mopuri**, and to my late brother-in-law, **Bayanna Mopuri**, for their support and for standing by me throughout my life and academic journey. I am equally grateful to all my family members for their unwavering support and belief in me. Last but not least, I would like to express my love and appreciation to my niece and nephew, **Sresta Mopuri** and **Sriram Mopuri**, whose innocence, laughter, and joyful spirits have brought immense happiness and warmth to our home.

Acronyms

ICE:	Internal combustion engine
CI:	Compression ignition
GHG:	Greenhouse gas
CO_2:	Carbon dioxide
NO_x:	Nitrogen oxides
PM:	Particulate matter
SO_x:	Sulphur oxides
HFO:	Heavy fuel oil
LFO:	Light fuel oil
MDO:	Marine diesel oil
IMO:	International maritime organization
DF:	Duel-fuel
LNG:	Liquefied natural gas
SCR:	Selective catalytic reduction
λ_{opt}:	Optimal wavelength
μ_L:	Dynamic viscosity of the liquid
ρ_L:	Liquid density
σ:	Liquid surface tension
d_j:	Initial jet diameter
MH:	Multi-hole
ASOI:	After start of injection
RMSE:	Root mean square error
CVPC:	Constant-volume pre-combustion cell
CPFR:	Constant pressure flow rig
CV-OSCC:	Constant-volume optical spray combustion chamber
HTC:	High temperature combustion
HTC:	Low temperature combustion

Contents

Part I

Overview

CHAPTER 1

Introduction and Literature Review

1.1 Pollutant emissions

In recent decades, increasing concerns about environmental sustainability and public health have brought the issue of harmful emissions from internal combustion engines (ICE) to the forefront of global discussions. These engines, widely used in the automotive, industrial, and maritime sectors, are favored for their efficiency, reliability, cost-effectiveness, and high energy density, making them essential in a wide range of applications. However, despite these advantages, they are also major contributors to greenhouse gas (GHG) emissions, such as carbon dioxide (CO_2), as well as nitrogen oxides (NO_x), particulate matter (PM), and sulfur oxides (SO_x) (G. C. Lazaroiu et al., 2024). Such emissions play a pivotal role in driving global warming, ocean acidification, and the deterioration of air quality, all of which have far-reaching consequences for ecosystems and human health (G. Lazaroiu and Mihaescu, 2021; Okajima and Kumagai, 1991). Maritime shipping occupies a particularly critical position among the various sectors dependent on combustion engines. According to the United Nations Conference on Trade and Development (UNCTAD), approximately 80% of global trade by volume and over 70% by value is transported by sea, establishing maritime transport as the backbone of international commerce (United Nations Conference on Trade and Development (UNCTAD), 2013). However, this vital industry is also a considerable source of GHG emissions. Currently, the sector accounts for approximately 3% of global GHG emissions, a figure that could rise to 17% by 2050 if stringent regulations are not implemented (Pereda et al., 2025). The maritime industry faces major challenges in dealing with environmental issues, mainly because it relies heavily on traditional fossil fuels and

operates on a global scale. To meet international environmental standards and encourage cleaner shipping, the International Maritime Organization (IMO) has set emission limits for ship engines, especially focusing on nitrogen oxides (NO_x) through its Tier I to Tier III regulations (International Maritime Organization, 2020).

1.2 Duel-fuel (DF) engine combustion

In response, various NO_x control strategies have been implemented, including advancements in combustion technology and the integration of selective catalytic reduction (SCR) systems in marine diesel engines. However, as emission regulations become increasingly strict in the coming years, the maritime industry will need to adopt emission control systems that are not only highly efficient but also compact and practical for use on ships. One significant drawback of SCR systems is that they require large quantities of liquid urea, which must be stored and carefully handled on board (Okubo and Kuwahara, 2020). This creates logistical challenges, particularly on vessels with limited space or those operating on long voyages where frequent resupply is not possible. As a result, there is a pressing need for alternative emission reduction technologies that can overcome these practical limitations while still achieving compliance with future regulations. Dual-fuel (DF) engines that operate on liquefied natural gas (LNG) are increasingly being recognized for their ability to reduce emissions in the maritime sector. These engines offer the flexibility to run on either LNG or traditional liquid marine fuels such as light fuel oil (LFO), heavy fuel oil (HFO), or even liquid bio-fuels. The use of LNG leads to a substantial and immediate reduction in emissions of carbon dioxide (CO_2), nitrogen oxides (NO_x), sulfur oxides (SO_x), and particulate matter (PM). According to findings, LNG can reduce SO_x emissions by up to 99%, PM_{10} and $PM_{2.5}$ by 95%, CO_2 by 41%, and NO_x by 82% (Karatuğ et al., 2023). As a marine fuel, LNG is already widely adopted globally, supported by established regulatory frameworks and a well-developed bunkering infrastructure. Dual-fuel systems also allow seamless switching between fuel types without compromising engine performance, enabling vessels to meet emission standards in regulated zones while optimizing fuel choice based on cost and availability (Wärtsilä, 2025). In dual-fuel (DF) compression ignition (CI) engines operating on natural gas, a small quantity of pilot fuel, typically diesel, is required to initiate combustion. Natural gas does not ignite under compression alone because it has a low cetane number and a high auto-ignition temperature compared to diesel. Therefore, without pilot fuel, natural gas cannot achieve reliable ignition in a compression ignition engine due to its high auto-ignition temperature and the typically lean air-fuel mixture (Chandra et al., 2011; Agarwal et al., 2022). To overcome this, a small quantity of diesel is injected near the end of the compression stroke. This pilot fuel ignites first due to the heat of compression, creating a localised high-temperature zone that then ignites the surrounding natural gas-air mixture. This ignition method ensures consistent combustion stability, maintains thermal efficiency, and effectively reduces NO_x and PM emissions across a wide range of loads and operating conditions (Pounder and Woodyard, 2004). Engine management systems regulate the gas-to-diesel ratio according to load, speed, and operating conditions. To effectively control NO_x emissions, limiting the amount of pilot fuel injected is crucial. Generally, maintaining pilot fuel below 5% at nominal load can reduce NO_x emissions to roughly one-tenth of those produced by conventional diesel engines (Wärtsilä Corporation, 2023; Sombatwong et al.,

2013). Reliable combustion depends on precise control of the pilot injection. Parameters such as injection timing, pilot fuel quantity, spray formation, and atomization characteristics are crucial in determining ignition quality, combustion stability, and emission levels in dual-fuel engines (Pounder and Woodyard, 2004). The efficiency and reliability of the combustion process depend heavily on the fuel atomization and vaporization behavior, along with its mixing with the surrounding air inside the combustion chamber. Factors such as injection pressure, ambient temperature, and in-cylinder gas density significantly influence spray atomization, droplet breakup, and fuel evaporation processes, which in turn affect mixture formation and combustion performance (Hiroyasu and Masataka Arai, 1990).

1.3 Liquid jet breakup and atomization regimes

The disintegration of liquid jets into droplets is a key process in fluid dynamics, with numerous applications in fuel injection, spray painting, agricultural sprays, and related fields. When a liquid jet exits a nozzle, it initially forms a continuous cylindrical stream. The interaction between cohesive forces within the liquid and external disruptive forces causes surface perturbations and oscillations. These perturbations grow in amplitude and eventually lead to the breakup of the liquid stream into individual droplets. The transition from a continuous jet to a spray involves two key stages, *primary atomization*, where the jet breaks into large droplets or ligaments, and *secondary atomization*, where these droplets further fragment into finer droplets due to aerodynamic or shear forces (Lefebvre and McDonell, 2017). Rayleigh (Rayleigh, 1878) mathematically described the jet instability by analyzing small perturbations on the liquid (non-viscous) surface. His work demonstrated that a liquid jet becomes unstable to axisymmetric perturbations when the wavelength λ exceeds the jet circumference $\pi\,\mathrm{d_j}$. The perturbations with wavelengths longer than this circumference will grow exponentially over time, causing the jet to break up. In other words, the jet becomes unstable when $\lambda > \pi\,\mathrm{d_j}$, where $\mathrm{d_j}$ is the diameter of the jet. Figure 1.1 illustrates the natural breakup of a liquid jet, where surface perturbations develop with irregular wavelengths. As a result, the jet disintegrates into a stream of droplets with varying sizes, some smaller and others larger than the nozzle orifice diameter. The perturbations in the jet that

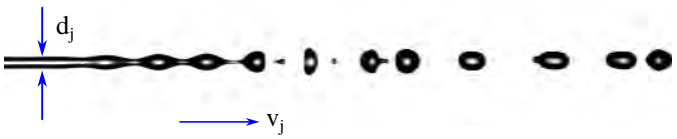

Figure 1.1: Natural jet disintegration, jet/orifice diameter ($\mathrm{d_j}$) = 100 µm (Lokesh, 2017).

exhibit the highest exponential growth rate occur at a wavelength of $\lambda_{\mathrm{opt}} = 4.51\,\mathrm{d_j}$, where $\mathrm{d_j}$ is the initial diameter of the jet. The amplification of these perturbations leads to the fragmentation of the jet into droplets with a characteristic diameter of $\mathrm{D} = 1.89\,\mathrm{d_j}$. Suppose periodic perturbations of appropriate wavelength λ and amplitude are applied to the liquid jet. In that case, it breaks into evenly spaced droplets of nearly equal size, as illustrated in Fig. 1.2. Although the droplets initially exhibit oscillatory behavior, they gradually attain

Figure 1.2: A laminar liquid jet, issued from an orifice with a diameter of $d_o = 100\,\mu m$, is subjected to regular, controlled perturbations at a frequency of $f_d = 12.0\,kHz$ (Lokesh, 2017).

a spherical shape as they move downstream, due to the combined effects of liquid viscosity and surface tension, as shown in Fig. 1.3. While foundational, this model was based on the

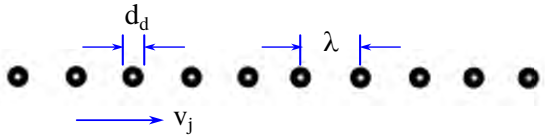

Figure 1.3: Mono-disperse droplets at downstream (Lokesh, 2017).

assumption of an inviscid and static environment, which limits its applicability to practical spray systems where viscous effects and aerodynamic interactions play a significant role.

Weber (Weber, 1939) extended Rayleigh (Rayleigh, 1878) theory by including the effects of both liquid viscosity and aerodynamic drag. He demonstrated that viscous damping slows the growth of instabilities, increasing the optimal perturbation wavelength. The corrected wavelength accounting for viscosity is given by Eqn. 1.1.

$$\lambda_{opt} = \sqrt{2\,\pi\,d_j}\left(1 + \frac{3\,\mu_L}{\sqrt{\rho_L\,\sigma\,d_j}}\right)^{0.5} \tag{1.1}$$

where, λ_{opt} is the optimal wavelength of the most unstable disturbance, d_j is the initial jet diameter, μ_L is the dynamic viscosity of the liquid, ρ_L is the liquid density, and σ is the liquid surface tension. As the liquid jet propagates through the surrounding air, aerodynamic forces impose shear stresses on its surface, inducing additional surface perturbations. Aerodynamic forces act to destabilize the liquid jet by introducing external air resistance, which reduces both the breakup length and the wavelength of surface disturbances. As a result, the jet undergoes an earlier breakup, producing smaller droplets due to the enhanced atomization process. For instance, increasing the relative air velocity from zero to 15 m/s could reduce the optimal wavelength from $4.44\,d_j$ to $2.8\,d_j$ (Lefebvre and McDonell, 2017).

Building upon the foundational theoretical developments of Rayleigh and Weber, Ohnesorge (Ohnesorge, 1936; Lefebvre and McDonell, 2017) introduced a comprehensive dimensionless framework to characterize the breakup behavior of liquid jets across a broad range of fluid properties and flow conditions. This framework incorporates three key dimensionless numbers: the Reynolds number, which represents the ratio of inertial to viscous forces in fluid flow; the Weber number, which denotes the ratio of inertial to surface tension forces;

and the Ohnesorge number, which accounts for the combined effects of viscosity, surface tension, and inertia in jet breakup phenomena. These parameters are defined as follows,

$$\mathrm{Re} = \frac{\rho_\mathrm{L}\, U\, \mathrm{d_j}}{\mu_\mathrm{L}} \tag{1.2}$$

$$\mathrm{We} = \frac{\rho_\mathrm{L}\, U^2\, \mathrm{d_j}}{\sigma} \tag{1.3}$$

$$\mathrm{Oh} = \frac{\mu_\mathrm{L}}{\sqrt{\rho_\mathrm{L}\, \sigma\, \mathrm{d_j}}} = \frac{\sqrt{\mathrm{We}}}{\mathrm{Re}} \tag{1.4}$$

where ρ_L is the liquid density, U is the jet velocity, $\mathrm{d_j}$ is the initial jet diameter, μ_L is the dynamic viscosity, and σ is the liquid surface tension. Collectively, these dimensionless groups quantify the relative influences of inertia, viscosity, and surface tension forces in determining the instability and breakup behavior of liquid jets. OhNumberchart.png

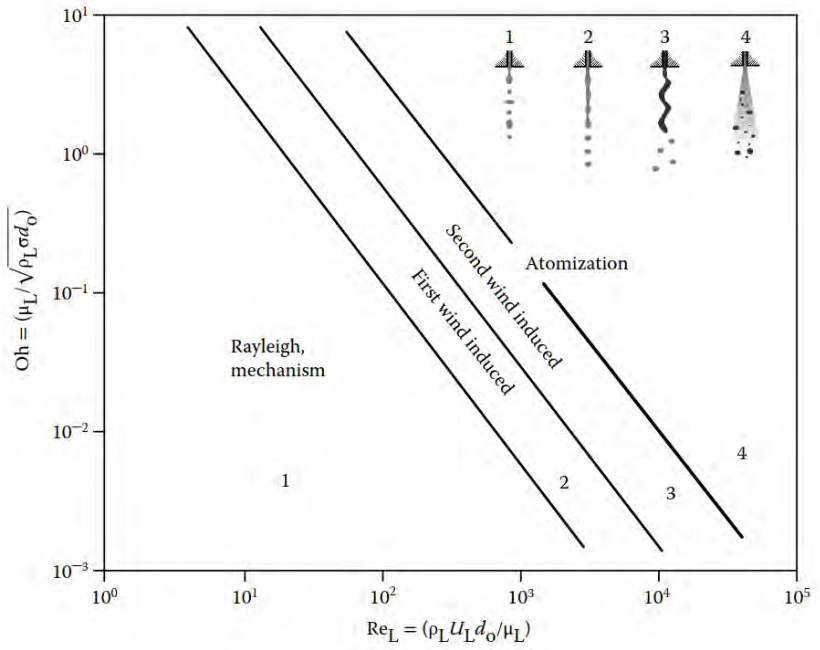

Figure 1.4: atomization and other breakup regimes of a liquid Jet (Lefebvre and McDonell, 2017).

Using this dimensionless framework, Ohnesorge systematically identified three principal jet breakup regimes. At low Reynolds and Ohnesorge numbers, breakup occurs in the classical Rayleigh regime, dominated by surface-tension-driven instabilities. As the Reynolds number increases to moderate values, aerodynamic interactions induce sinuous oscillations on the liquid column, promoting asymmetric wave development and producing a broad droplet size distribution. At high Reynolds and Weber numbers, inertial and aerodynamic forces be-

come dominant, leading to rapid atomization and the formation of fine sprays immediately downstream of the nozzle.

Integrating these developments, Reitz Reitz, 1978 formulated a comprehensive atomization regime map that connected fundamental instability mechanisms to practical spray behaviors as shown in Fig. 1.4. His model distinguished four regimes: Rayleigh breakup, where surface tension dominates and droplets form with $D \approx 1.89\,\mathrm{d_j}$; first wind-induced breakup, where moderate Weber numbers cause surface waves and droplets roughly the size of the jet diameter; second wind-induced breakup, where shear-driven instabilities produce much finer droplets ($D \ll \mathrm{d_j}$); and atomization, where high Weber and Reynolds numbers trigger turbulent disintegration near the nozzle exit. The critical condition for transition to atomization was identified as $\mathrm{We}_\lambda > 13$, where We_λ is the Weber number based on perturbation wavelength.

1.4 Fuel spray studies in combustion engines

Atomization is the process of breaking a continuous liquid stream into fine droplets, which are then dispersed within a surrounding gas. This process is essential because it significantly increases the liquid surface area, enhancing its interaction with the surrounding environment (Lefebvre and McDonell, 2017). Atomization plays an important role in a wide range of industrial and scientific applications. For instance, in agriculture, it allows the efficient spraying of fertilizers and pesticides over crops. In meteorology, atomization helps in understanding natural phenomena such as mist and rain (Ashgriz, 2011). In the medical field, it facilitates the delivery of medication through devices like inhalers and nebulizers (Mohandas et al., 2021). Furthermore, in various engineering systems, particularly combustion engines and cooling technologies, precise control over droplet size and distribution is crucial for achieving optimal performance and efficiency.

Atomization occurs through one of three mechanisms: the kinetic energy of the liquid, the aerodynamic force of high-velocity air or gas, or the mechanical energy imparted by a rotating or vibrating device. This process is fundamental to the combustion of liquid fuels in diesel engines, spark-ignition engines, gas turbines, rocket engines, and industrial furnaces. It increases the specific surface area of fuel droplets, enhancing mixing with the surrounding air and accelerating evaporation (Lefebvre and McDonell, 2017). Proper atomization is essential for achieving stable combustion, efficient heat release, and minimized emissions. Figure 1.5 illustrates the sequence of atomization processes and the characteristic features of a spray. Optical imaging techniques have been used for decades to investigate automotive fuel sprays and combustion processes, with applications in both academic research and industry. To replicate the high-pressure and high-temperature conditions present inside combustion engines, researchers have developed specialized spray test rigs capable of operating under engine-relevant conditions (Baert et al., 2009; Raul Payri, García-Oliver, et al., 2012; Bardi et al., 2012). These test setups incorporate advanced optical diagnostics that enable precise visualization and analysis of spray behavior.

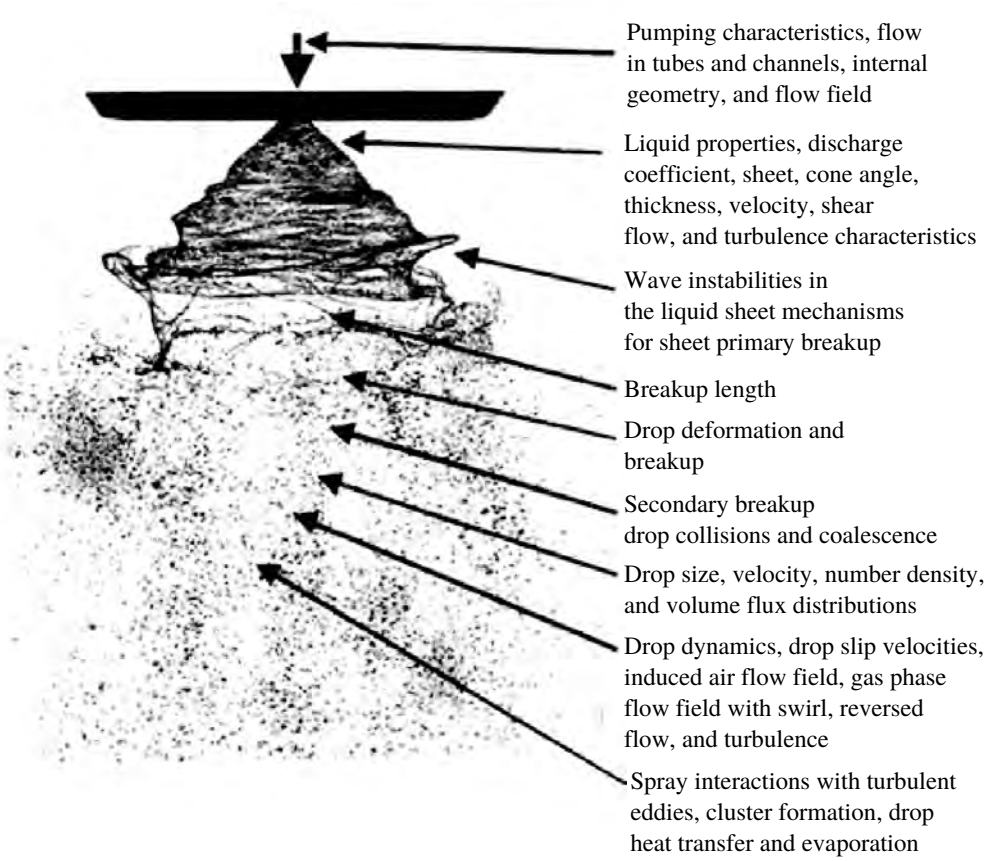

Figure 1.5: An overview of the various stages involved in spray atomization (Lefebvre and McDonell, 2017).

1.4.1 Spray visualization test rigs

The primary function of spray visualization test rigs is to replicate the thermodynamic conditions present within internal combustion engines during fuel injection and combustion. This controlled simulation is essential for accurately observing and analyzing spray behavior under engine-relevant conditions. Various configurations of spray test rigs are currently in use worldwide, each tailored to specific research objectives and engine types. An overview of the major types of test rigs commonly employed in spray and combustion research is provided below. The most widely adopted test rigs are the constant-volume hot cell, CVHC (Du et al., 2017; Deshmukh, 2011), constant-volume pre-combustion cell, CVPC (Baert et al., 2009; Bardi et al., 2012), and constant-pressure flow rig, CPFR (Bardi et al., 2012; Raul Payri, García-Oliver, et al., 2012). These systems are specifically designed to produce the controlled high-pressure and high-temperature environments necessary to investigate fuel spray behavior, combustion characteristics, and air-fuel mixing under conditions representative of actual engine operation.

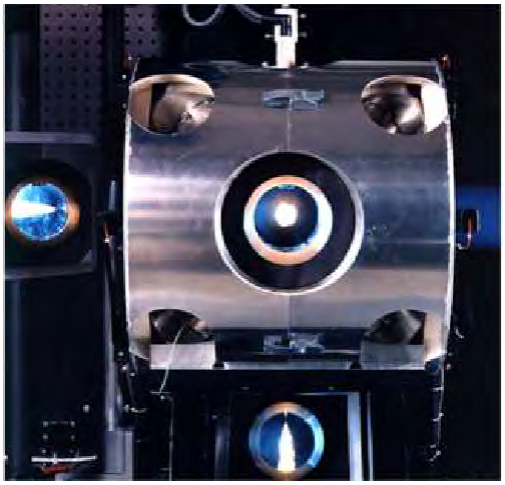

(a) CVPC (Sandia)

(b) CPFR (CMT)

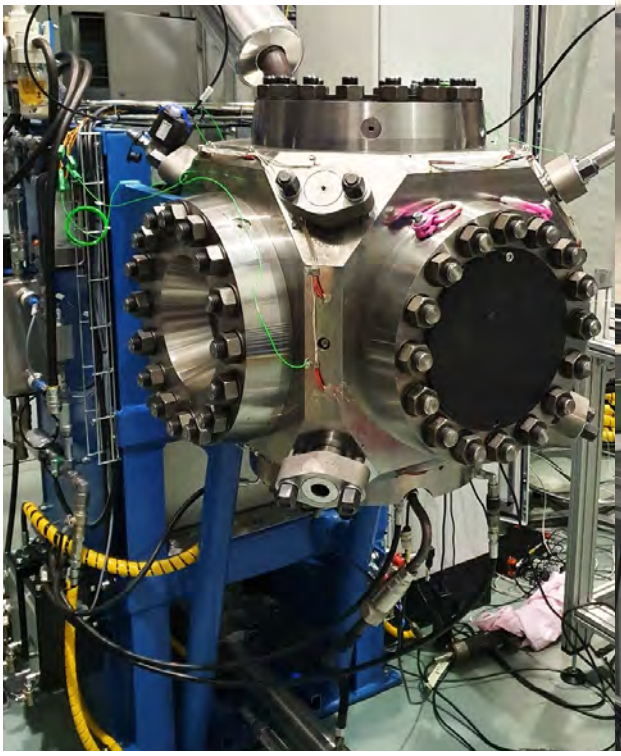

(c) CV-OSCC (Wärtsilä)

(d) CPFR (Chalmers)

Figure 1.6: Spray test rigs: (a) Constant-volume pre-combustion cell (CVPC) at Sandia National Laboratory (Bardi et al., 2012), (b) Constant pressure flow rig (CPFR) at Universitat Politècnica de València – CMT-Motores Térmicos (Bardi et al., 2012), (c) Constant-volume optical spray combustion chamber (CV-OSCC: pre-mixed combustion chamber) at Wärtsilä corporation, (d) Constant-pressure flow (CPFR) rig at Chalmers University of Technology.

Constant-volume hot cell (CVHC) functions by pressurizing a sealed chamber with gas. Inert gases are typically used for spray studies, while air is used for combustion experiments. An internal electric heating element raises the temperature of the pressurized gas to the required level. Once both the pressure and temperature reach the set values, the fuel injector is activated to initiate the injection process. Despite its advantages, the CVHC has certain limitations. Prolonged exposure to high temperatures causes degradation of the O-ring seals, leading to potential gas leakage. Additionally, efficient cooling of the fuel injector is essential to prevent thermal damage during operation. The maximum achievable temperature within the CVHC is also restricted by the material limitations of the heating elements (Pal, 2019). The limitations of the CVHC in handling high temperatures were resolved by incorporating a constant-volume pre-combustion cell (CVPC). In this system, a premixed, lean combustible gas mixture is introduced into a sealed chamber. The mixture is ignited by a spark plug, and the resulting combustion rapidly increases the pressure and temperature of the chamber to the desired levels. The mixing fan is operated both before and after ignition to ensure a uniform temperature distribution and a consistent gas composition throughout the chamber. Once the target thermodynamic conditions are reached, the fuel is injected into the chamber. The subsequent spray and combustion events are observed and recorded through optical windows. The constant pressure flow rig (CPFR) differs from the CVHC and CVPC by providing a continuous flow of high-pressure, preheated gas into the test section. This system maintains a constant ambient pressure during the entire injection process. Compressed gas is stored in a high-pressure reservoir, heated using electric resistance heaters, and then supplied to the chamber. The CPFR is particularly suitable for experiments that require steady-state boundary conditions. The system operates in two distinct modes. In the open-loop configuration, a continuous inflow and outflow of gas is maintained throughout the experiment, enabling the chamber to function as a constant-pressure flow (CPF) system. In contrast, the closed-loop configuration involves initially filling the chamber with gas to the required thermodynamic conditions, after which no further gas exchange occurs during fuel injection. This setup allows the chamber to behave as a constant-volume system.

In addition to these rigs, two other rigs are commonly used in combustion research: the rapid compression machine (RCM) and the optical research engine (ORE) (Mittal et al., 2011). The RCM achieves the desired pressure and temperature conditions through a single, rapid piston stroke that compresses the gas mixture to top dead center (TDC). The resulting combustion occurs at constant volume, allowing a detailed study of ignition delay and combustion characteristics. However, RCMs are expensive and complex to operate. Mechanical vibrations at the end of the compression stroke pose challenges for applying sensitive laser-based optical diagnostics (Baert et al., 2009). The optical research engine (ORE) offers a more realistic simulation of in-cylinder conditions compared to static chambers and RCMs. It is essentially a real engine modified with optical access ports made of quartz or sapphire, allowing direct visualization of fuel injection, spray formation, ignition, and combustion inside the cylinder. The ORE setup allows detailed investigation of spray/wall, spray/piston, and spray/spray interactions, making it the closest representation of actual engine behavior among all available experimental test rigs (Phan, 2009). However, due to their structural complexity, high operational costs, risk of optical window fouling, and the ORE need for careful design integration to accommodate diagnostic tools. The CVHC, CVPC, and CPFR rigs provide controlled, repeatable environments for fundamental spray

and combustion studies; the RCM and ORE systems offer complementary advantages.

1.4.2 Spray and spray flame characteristics

As outlined in earlier sections, spray atomization is the process by which a liquid fuel jet is disintegrated into millions of fine droplets, significantly enhancing evaporation and promoting the formation of a homogeneous fuel–air mixture in vapor form. The quality of this mixture is critical for achieving efficient combustion and reducing emissions in internal combustion engines. Research on fuel sprays covers both non-evaporative and evaporative sprays in non-reactive environments, as well as reactive sprays involving combustion processes. A comprehensive understanding of spray morphology requires the characterization of both macroscopic and microscopic spray properties. Macroscopic parameters include spray tip penetration, spray cone angle, and projected spray area, which describe the overall shape and extent of the spray plume. Microscopic parameters involve measurements of droplet size and velocity distributions, along with their statistical averages (Agarwal et al., 2022). In non-reactive conditions, studies have primarily focused on quantifying these macroscopic and microscopic characteristics to understand the physical dispersion and evaporation behavior of the spray. In contrast, reactive spray investigations emphasize parameters that capture the interaction between spray dynamics and combustion phenomena, including ignition delay, lift-off length, flame structure, heat release rate, and pollutant formation under various injection and ambient conditions (Agarwal et al., 2022).

1.4.2.1 Non-reactive sprays

Non-evaporative sprays

In spray research, a non-evaporative ambient refers to conditions where the surrounding gas is maintained at ambient temperature to prevent the evaporation of the fuel spray. This ensures that the spray remains entirely in the liquid phase, enabling the investigation of its physical structure and aerodynamic behavior without the influence of evaporation. Under such non-evaporative conditions, experimental studies have consistently shown that an increase in the ambient gas density reduces the spray tip penetration and increases the spray cone angle. This is because higher gas density produces greater aerodynamic resistance against the spray, which slows down its forward movement and causes it to spread more widely in the lateral direction. This behavior is primarily attributed to the enhanced aerodynamic drag exerted by the denser ambient gas, which decelerates the spray tip more rapidly and promotes greater lateral dispersion of the spray (Naber and Dennis L Siebers, 1996; X. Wang et al., 2010; R. Payri, F. Salvador, et al., 2011; Raul Payri, Jaime Gimeno, De la Morena, et al., 2016). Along with ambient conditions, injection pressure is a key parameter that influences spray behavior. It has a strong influence on spray break-up and mixing with ambient air. Liquid fuel jets/sprays are disintegrated into fine droplets due to the relative velocity between the spray and the ambient gas. With an increase in the injection pressure, the nozzle outlet velocity also increases, favoring the production of smaller droplets and improved atomization (M. Arai et al., 1984). Several studies have reported that higher injection pressure enhances the spray tip penetration and spray volume but hardly affects the spray cone angle, which remains relatively constant during the entire

injection process (Delacourt et al., 2005; Kim et al., 2013). This observation indicates that although the injection pressure highly effectively enhances spray penetration, it does not fundamentally alter the spray cone angle. Furthermore, higher injection pressures produce greater spray tip velocities due to greater momentum at the nozzle exit before the spray tip reaches its maximum velocity (Kim et al., 2013).

Evaporative sprays

An evaporative spray environment is established either by heating the surrounding gas to the desired temperature and pressure or by employing a pre-mixed combustion process that, once completed, leaves behind a high-temperature, high-pressure, inert atmosphere. Under these evaporative conditions, the injected liquid fuel penetrates only up to a certain axial distance from the injector. Beyond this point, the tip of the liquid core of the spray no longer advances steadily; instead, it fluctuates around a quasi-stationary axial position. Meanwhile, the vaporized portion of the spray continues to move downstream, with vapor-phase penetration progressing further even as the liquid-phase tip remains near the same location (Espey and Dec, 1995; Zheng et al., 2015). This phenomenon introduces a critical distinction in the characterization of evaporative sprays, wherein the liquid-phase penetration is treated as a separate parameter, commonly referred to as the liquid length (LL). Liquid length is defined as the maximum axial distance from the injector nozzle to the furthest extent of the liquid-phase fuel within the spray. Accurate determination of LL is of particular importance in engine design, as excessive liquid penetration may result in impingement on the piston crown or cylinder liner (spray–wall interaction). Spray–wall interaction describes the behavior of fuel sprays upon impingement with the combustion chamber surfaces. This interaction plays a crucial role in influencing the secondary evaporation of fuel droplets or the formation and evaporation of wall films, both of which significantly impact soot and unburned hydrocarbon (HC) emissions in internal combustion engines (Moreira et al., 2010; Agarwal et al., 2022).

The liquid length (LL) of evaporating diesel sprays is influenced by several factors related to nozzle geometry, ambient conditions, and fuel properties. It has been established that liquid length increases linearly with orifice diameter, as a larger nozzle produces a thicker liquid core that extends further before breakup occurs (Dennis L. Siebers, 1998; Desantes et al., 2005). In contrast, increasing the ambient gas density leads to a reduction in liquid length. A denser ambient environment accelerates spray breakup and enhances atomization, which promotes faster fuel evaporation and shortens the liquid penetration. Additionally, higher ambient density increases the entrainment of hot surrounding gases into the spray, further contributing to the reduction of liquid length (Dennis L. Siebers, 1998; Jaime Gimeno et al., 2016; Raul Payri, Juan P. Viera, et al., 2017). Ambient gas temperature also plays a crucial role in determining liquid length. As ambient temperature rises, the thermal energy available in the surrounding gas increases, causing the entrained air to heat the liquid fuel more rapidly. This elevated heating enhances the fuel vaporization rate, resulting in a shorter liquid phase penetration within the spray (Dennis L. Siebers, 1998; Raul Payri, Juan P. Viera, et al., 2017). At a given ambient temperature, a shorter liquid length typically indicates more efficient and faster air-fuel mixing, which is desirable for improving combustion quality and reducing emissions (Espey and Dec, 1995). In contrast to ambient conditions, injection pressure has been found to have little to no significant

effect on liquid length. Although higher injection pressure increases the fuel injection rate and sprays momentum, it simultaneously promotes greater air entrainment in proportion, thereby maintaining the overall energy balance and leaving liquid length largely unchanged (Dennis L. Siebers, 1998; Desantes et al., 2005; Raul Payri, Juan P. Viera, et al., 2017). Furthermore, fuel temperature and volatility are important fuel-related factors influencing liquid length. An increase in fuel temperature or the use of fuels with higher volatility leads to a reduction in liquid length by accelerating fuel heating and vaporization processes (Canaan et al., 1998; Raul Payri, García-Oliver, et al., 2012). Finally, for multi-component fuels, the liquid length is primarily governed by the least volatile components in the mixture, as these fractions evaporate more slowly and therefore dictate the final extent of the liquid core (Jaime Gimeno et al., 2016). The procedure for determining liquid length in sprays has

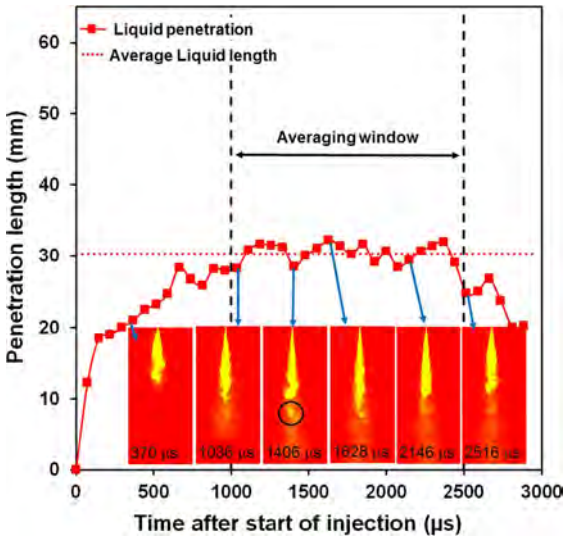

Figure 1.7: Liquid length measured at different times after start of injection (SOI). The threshold for optical thickness was set at $\tau = 0.6$ (Pal, 2019).

been well-documented by the Engine Combustion Network (ECN) (Jung et al., 2015), and is widely adopted in experimental spray research. Images obtained through DBI techniques were converted to binary form by applying a threshold based on optical thickness. Initially, the intensity value at each pixel in the spray image, denoted as $\mathrm{I}(x, y)$, was normalized by dividing it by the intensity at the corresponding pixel in the background image, $\mathrm{I_{BG}}(x, y)$. The background was created by averaging ten images captured prior to the start of injection (SOI):

$$\mathrm{I_n}(x, y) = \frac{\mathrm{I}(x, y)}{\mathrm{I_{BG}}(x, y)}$$

The optical thickness τ at each pixel is then calculated as the negative logarithm of the normalized intensity:

$$\tau(x, y) = -\log\left[\mathrm{I_n}(x, y)\right]$$

Figure. 1.7 presents the liquid length values determined using a threshold of $\tau = 0.6$ at various times after the start of injection. The average liquid length was obtained by taking

the mean of values recorded between 1 ms and 2.5 ms after SOI. All these sprays have been studied during longer injection durations, with the liquid length measured under steady-state conditions. However, this approach does not apply to transient sprays, where the spray does not reach a steady state.

1.4.2.2 Reactive sprays

High-speed imaging has become an indispensable diagnostic tool for examining highly transient combustion phenomena, especially in processes like diesel spray injection and combustion. Techniques such as shadowgraph, schlieren imaging, and natural luminosity imaging provide crucial information about spray penetration, spray cone angle, ignition delay, ignition location, and soot formation characteristics (Lyle M. Pickett et al., 2009). This experimental data is essential for the development, validation, and refinement of multi-dimensional computational fluid dynamics (CFD) models tailored for spray combustion applications. These validated models are subsequently employed for optimizing the design and performance of next-generation high-efficiency, low-emission engines. In the combustion sequence of diesel spray compression ignition, two primary stages are typically observed: low temperature combustion (LTC), also referred to as cool flame or warm flame (first-stage ignition), and high temperature combustion (HTC), known as hot flame (second-stage ignition) (Musculus et al., 2013). Notably, several researchers have proposed an additional intermediate stage within this process, termed intermediate temperature combustion (ITC), thereby dividing diesel ignition into three sequential phases: LTC, ITC, and HTC. In this classification, both LTC and ITC phases occur prior to the establishment of the high temperature flame (Ong et al., 2021; Y. Ju, 2021). The ignition characteristics during these initial stages play a decisive role, as they significantly influence the stability, properties, and limits of HTC, which in turn directly affects engine performance and emission behavior (D. Wang et al., 2023). Among the key parameters governing fuel spray combustion, ignition delay and lift-off length are particularly critical, as they directly determine engine efficiency and emission outcomes. Ignition delay, defined as the time gap between the start of fuel injection and the onset of combustion, tends to decrease with rising ambient temperatures and pressures due to accelerated chemical reaction rates. Similarly, lift-off length, the axial distance from the injector tip to the location of a stabilized flame, is also shortened under higher oxygen concentrations and increased ambient pressures (Senecal et al., 2003). Furthermore, elevating the fuel injection pressure enhances atomization quality and spray penetration, leading to reductions in both ignition delay and lift-off length. This behavior was comprehensively validated through CFD simulations, which confirmed that increased injection pressures improve combustion efficiency and result in shorter liquid lengths and flame lift-off distances (Senecal et al., 2003).

1.4.2.3 Near field spray atomization

Ballistic imaging is an optical diagnostic technique, originally developed for medical imaging, that has been adapted for visualizing dense liquid fuel sprays. The method captures ballistic photons, those that pass through the dense spray with minimal scattering, while filtering out multiply scattered photons. This is achieved using ultra-fast time-gated devices, such as Kerr gates or intensified cameras, which act as optical shutters. These shutters

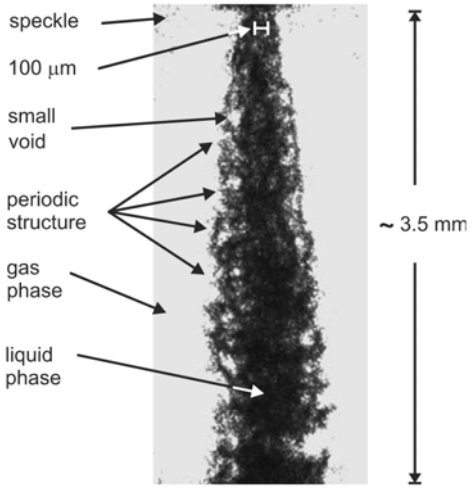

Figure 1.8: A ballistic image depicting the spray core, where dark areas correspond to the fluid phase and lighter areas indicate the gas phase (M. Linne et al., 2006).

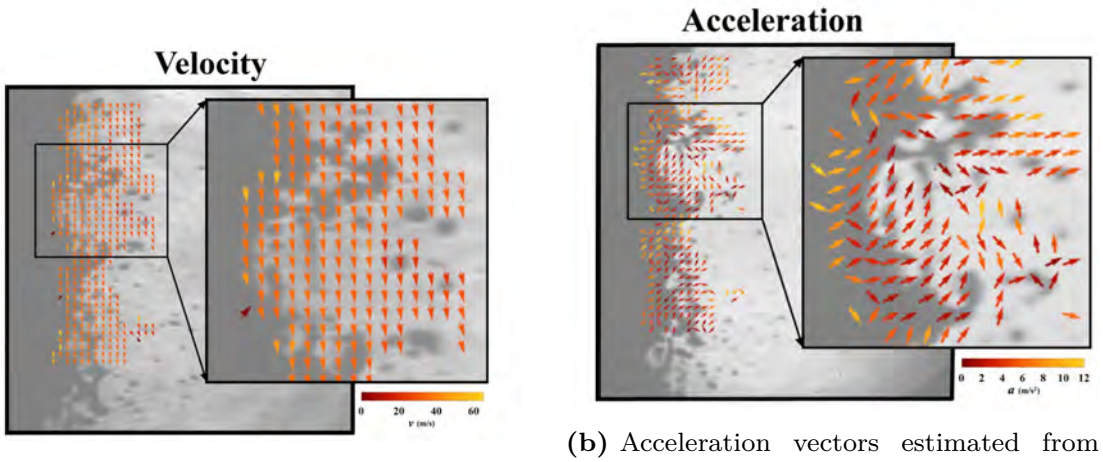

(a) Velocity vectors obtained by correlating selected regions (75 × 75 pixels) between successive images. Vector magnitudes are represented by a color scale, where red indicates the lowest and yellow the highest, reaching up to 65 m/s.

(b) Acceleration vectors estimated from time-resolved ballistic images, showing the forces acting within the spray. The color scale depicts vector magnitudes, with red denoting the minimum and yellow the maximum acceleration, reaching approximately 12 m/s^2.

Figure 1.9: Velocity and acceleration vector fields derived from ballistic imaging, capturing the dynamic motion and forces within the spray structure (Sedarsky et al., 2016).

allow only the earliest arriving photons, which experience the least interaction with spray droplets, to be recorded by the detector. As a result, ballistic imaging provides high spatial and temporal resolution images of near-nozzle spray structures, enabling detailed examination of initial breakup processes and transient features of the spray that are typically masked in conventional imaging methods due to extensive light scattering (M. Linne et al., 2006). As shown in the Fig. 1.8, periodic patterns are clearly visible in the core region of the spray. Faint traces of small ligaments are also noticeable. Moreover, once the jet becomes fully developed, regular voids appear along the outer boundary of the spray, indicating an organized breakup mechanism (M. Linne et al., 2006). In further extension studies by Sedarsky et al., 2016, targeted region-matching analysis was combined with the detection of image triplets to generate time-resolved velocity and acceleration vectors, representing the motion and forces involved in the spray development process, as shown in Fgs. 1.9a and 1.9b.

1.5 Motivation

In dual-fuel engines, the ignition process is initiated by a small quantity of liquid pilot fuel injection, which ignites the premixed LNG–air charge. Consequently, the behavior of the pilot spray, particularly its ignition characteristics and interaction with the gaseous environment, becomes a critical factor influencing overall engine performance, ignition reliability, and emission formation. Over the years, extensive research has been conducted on fuel sprays with longer injection durations (typically on the order of milliseconds) under automotive diesel engine conditions. These studies, using optically accessible engines and constant volume combustion chambers, have provided detailed data on spray penetration, liquid length, spray cone angle, vaporization, ignition delay, and flame lift-off length (Lyle M Pickett et al., 2010). However, pilot sprays in LNG dual-fuel marine engines differ fundamentally from these automotive main sprays. Pilot sprays involve short injection durations and much smaller fuel quantities, designed solely to initiate ignition rather than supply the primary energy. Such sprays operate in a ballistic needle regime, leading to distinct atomization, entrainment, and ignition characteristics when compared to longer, main injections (Frühhaber et al., 2018). A notable limitation in existing spray studies is that most investigations on automotive sprays have been performed using research injectors or customized nozzles, often modified into a single-hole configuration, to generate an isolated single spray plume. This is essential because multi-hole injectors typically produce multiple spray plumes, and interactions between neighboring plumes (plume-to-plume interference) introduce complexities in optical measurements, making it difficult to isolate individual spray behaviors (Raul Payri, F. J. Salvador, et al., 2020). These studies were typically conducted under high-temperature, high-pressure conditions in controlled constant volume chambers, using single-hole research nozzles to avoid interference effects. Recognizing this challenge, the present study adopts a new approach wherein a thimble type arrangement has been implemented to physically isolate a single spray plume from a multi-hole marine injector. This enables precise, optical characterization of an individual pilot spray plume without interference from adjacent plumes, providing reliable and representative data on spray morphology, penetration, ignition delay, and flame development under both non-reactive and reactive conditions.

Although extensive data exist for long, steady-state sprays in automotive diesel engines, experimental research on short-duration, transient/pilot sprays in LNG dual-fuel marine engines remains limited. There is a significant lack of optical diagnostic studies conducted under conditions relevant to marine engines. The injectors are designed for continuous, long-duration operation, but in dual-fuel mode, they are subjected to transient, short-duration pilot injections. As a result, the transient spray development, ignition site formation, and the influence of ambient pressure and temperature under these conditions have not been thoroughly investigated. Existing automotive data on vapor penetration and flame behavior cannot be directly applied to dual-fuel marine engines because of fundamental differences in injection duration, ambient conditions, and operating strategies.To address these gaps, this study performs a high-speed optical investigation of isolated pilot sprays under engine-relevant conditions to replicate dual-fuel marine engine environments. Mie-scattering, diffused backlight imaging, Schlieren, and natural luminosity imaging are employed to capture transient spray and combustion behavior. Additionally, the near-field spray structure is analyzed using ballistic imaging at different ambient and injection pressures.

1.6 Objectives

The primary aim of this research is to investigate the transient behavior of pilot fuel sprays in heavy-duty diesel injectors under conditions relevant to dual-fuel marine engine applications. The experiments were carried out using high-pressure and high-temperature spray test rigs using various optical diagnostics methods. The specific objectives of the study are as follows:

- The study developed and applied a plume isolation technique employing a thimble structure to isolate individual spray plumes from a multi-plume spray, effectively avoiding interference from adjacent spray plumes.
- The study examined plume-to-plume variations in multi-hole injectors under non-evaporative and non-reactive conditions, to assess the consistency and symmetry of spray formation across various injectors.
- Single-plume spray experiments were performed under non-evaporative and non-reactive conditions at various back pressures and injection pressures. Additionally, evaporative and non-reactive sprays were investigated across a range of back pressures, injection pressures, and ambient temperatures to analyze spray behavior under different thermodynamic conditions.
- The reactive behavior of the spray was studied under various ambient conditions and different oxygen concentrations to understand the transient spray combustion characteristics.
- The study investigated near-field atomization dynamics using time-resolved ballistic imaging, with particular emphasis on spray breakup and evolution within 10 mm of the nozzle, under ambient and various injection pressure conditions.

CHAPTER 2

Experimental Setup and Approach

The experiments were carried out in optically accessible spray test rigs to investigate the transient characteristics of fuel sprays over a range of fuel injection pressures, ambient densities, and temperatures. Various optical diagnostic techniques were employed to capture and analyze the spray dynamics. The spray characteristics are examined under the following conditions:

- **Phase-I**: Non-evaporative, non-reactive sprays
- **Phase-II**: Evaporative, non-reactive sprays
- **Phase-III**: Reactive sprays
- **Phase-IV**: Near-field spray atomization using ballistic imaging

2.1 Spray visualization test rigs

2.1.1 Constant volume optical spray combustion chamber (OSCC)

The Optical Spray Combustion Chamber (OSCC) is a constant-volume, pre-mixed combustion test rig (Fig. 2.1) designed for detailed optical diagnostics of fuel spray and combustion studies under precisely controlled conditions. The chamber features a cubical shape with an internal volume of 17.2 liters and includes several modular components such as a gas exchange system, injector adapter, corner modules, and three optical quartz windows. These windows facilitate a selection of optical diagnostic techniques based on experimental needs.

Parameter	**Value / Description**
Outer dimensions	600 × 600 × 550 mm
Internal volume	0.0172 m^3 (17.2 litres)
Operating pressure	0–400 bar
Chamber body temperature	20–200 °C
Operation mode	Closed (constant-volume chamber)
Spray Type	
Cold phase	Non-reactive sprays
Hot phase	Reactive sprays
Heat and Pressure Generation	
Cold phase	Pressurized air
Hot phase	Pre-mixed combustion

Table 2.1: Characteristics of the optical spray combustion chamber (OSCC).

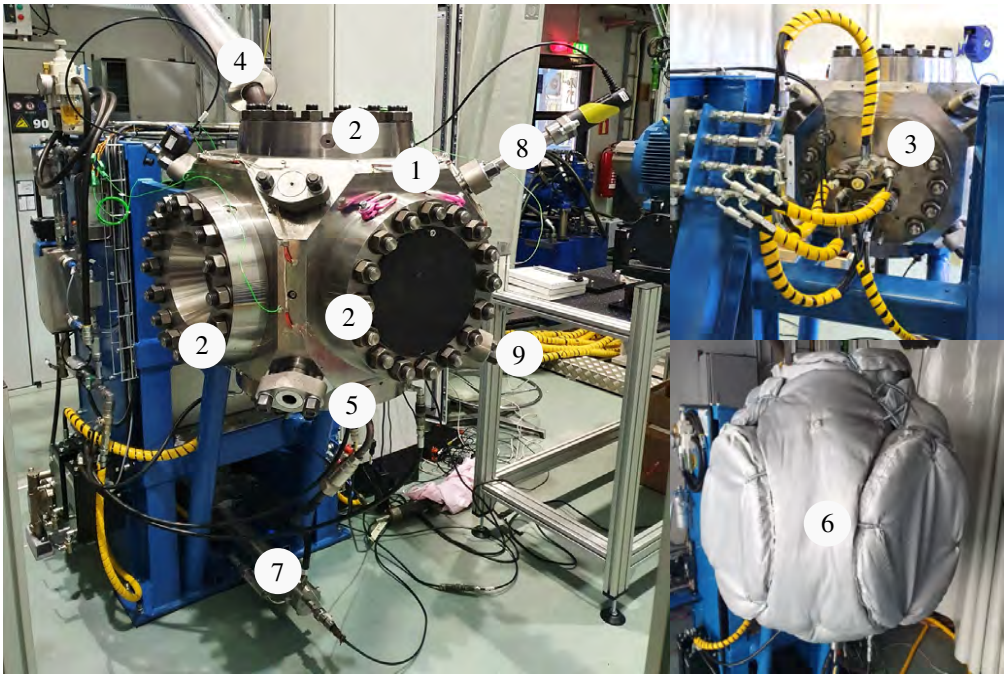

Figure 2.1: Optical spray combustion chamber (OSCC) components: (1) chamber body, (2) window module, (3) gas exchange module-inlet, (4) gas exchange module-exhaust, (5) injector module, (6) insulation for the hot phase (7) fuel supply system, (8) corner module-spark plug, (9) corner modules for internal pressure and temperature measurements.

The injector is mounted at the bottom of the chamber, positioned vertically to capture all spray plumes simultaneously, and can also be tilted at an angle to study individual

spray plumes. The chamber can operate in a cold mode, without heating, to investigate non-evaporative and non-reactive sprays. In this mode, the desired pressure is maintained by filling the chamber with compressed air through the gas exchange modules, while temperature remains at ambient levels. For evaporative and reactive spray experiments, the chamber temperature is increased using a pre-mixed combustion process. This is initiated by a spark plug installed in a corner module, which ignites a fuel-air mixture to raise the temperature before fuel injection. Pressure and temperature inside the chamber are continuously monitored via sensors in the corner modules. Temperature measurements are taken at two locations: near the nozzle tip $T_1$and at the top corner of the chamber T_2. The chamber's operating temperature is then calculated as the average of these two readings, the specifications of the OSCC are listed in Table 2.1. These temperatures were measured using a specially designed thin thermocouple, which responds rapidly to temperature changes due to its low thermal mass. To keep the experimental conditions consistent, the chamber was emptied and refilled using the exhaust and inlet valves. In non-evaporative and non-reactive spray tests, this was done after every five sprays to reduce the chance of leftover fuel mist affecting the spray pattern. In tests with evaporative and reactive conditions, the chamber was emptied and refilled with fresh gas mixtures before every spray. The viewing windows were cleaned whenever needed, based on visual checks and the clarity of the images captured.

2.1.2 Constant-pressure flow (CPF) chamber

The constant-pressure flow (CPF) chamber is an optically accessible, high-pressure vessel. The chamber operates in two modes: open-loop and closed-loop. In open-loop mode, compressed gas enters through an inlet at the bottom and flows upward, exiting via an exhaust outlet at the top, creating a continuous flow through the chamber. In closed-loop mode, the chamber functions as a constant-volume vessel with no continuous gas flow, maintaining a stable pressure similar to an OSCC setup. The CPF chamber is suitable for both cold and hot phase operations. In cold-phase tests, ambient temperature is maintained while the desired back pressure is achieved using compressed air. For hot-phase operation, elevated

Parameter	**Value / Description**
Injector position	Mounted on the side of the chamber
Gas inlet	Bottom of the chamber
Gas exhaust	Top of the chamber
Operating Modes	
Open-loop mode	Continuous gas flow from bottom inlet to top exhaust
Closed-loop mode	No continuous flow, constant-volume operation
Spray Type	
Cold phase	Non-reactive sprays
Hot phase	Reactive sprays

Table 2.2: Characteristics of the constant-pressure flow (CPF) chamber.

Figure 2.2: Components of the constant-pressure flow (CPF) chamber: (1) ICCD camera, (2) injector module, (3) fuel supply system, (4) gas exchange module—inlet, (5) gas exchange module—exhaust, (6) nozzle tip.

temperatures are generated by igniting a pre-mixed fuel–air mixture inside the chamber before fuel injection, allowing investigation of evaporative and reactive sprays under high-temperature conditions. In the present study, the CPF chamber was operated in cold-phase conditions, maintaining ambient temperature while applying elevated back pressures with compressed air. The injector is mounted on the side wall of the chamber, enabling clear visualization of spray plumes and near-field atomization. Pressure and temperature sensors are installed to continuously monitor and control the internal environment, ensuring consistent and reliable test conditions, the specifications of the CPF are listed in Table 2.2.

2.2 Test matrix and the injectors details

Table 2.3 summarizes the spray types, injectors used, nozzle/plume configurations, diagnostic techniques applied for each case, and categories of experiments conducted. The properties of these fuels tested in this study are listed in Table 2.4. The first phase of the experiments focused on non-evaporative, non-reactive spray conditions. Initially, tests were performed using injector-A1 to study spray behavior with three different nozzle setups. In the first setup, adjacent nozzle holes were welded shut to produce an isolated spray plume,

Test	Spray type	Injectors	Nozzle/plume configuration			Diagnostics	Fuel
			Isolated spray (single spray)		Multi-plume		
			Welded nozzle (plume-blocking)	Thimble method (plume-thimble)	MH nozzle (plume1-9)		
1	Non-evaporative and non-reactive	A1	✓	✓	✓	DBI, Mie-scattering	LFO
		A1, A2, B and C	✗	✓	✓		
2	Evaporative and non-reactive	B	✗	✓	✗	DBI, Schlieren	n-heptane
3	Reactive	B	✗	✓	✗	Schlieren and Luminosity	
4	Near field atomization	A1	✓	✗	✗	Ballistic imaging	Diesel

Table 2.3: Summary of experiments: spray types, injectors, nozzle configurations, and diagnostic techniques used.

allowing the study of a single plume without interference from others. The second setup used the thimble method, where surrounding holes were covered to isolate a single plume without changing the nozzle shape. The third setup used a multi-hole (MH) nozzle with all holes open, creating a multi-plume spray to observe interactions between plumes. Diffuse back-illumination (DBI) imaging was used to capture single plumes, while Mie-scattering imaging was used for multi-plume sprays. In addition, four similar injectors (A1, A2, B, and

Property	LFO	n-heptane	Diesel
Density @ 15 °C (kg/m^3)	833.5	684	840
Viscosity @ 40 °C (mm^2/s)	3.036	0.41	3.0
Flash Point (°C)	64.5	−4	64
Sulfur (mg/kg)	< 10	–	< 10

Table 2.4: Fuel properties (Wärtsilä Corporation, 2023).

C) were tested under the same non-evaporative, non-reactive conditions to compare their spray characteristics and variability among the injectors. Multi-plume sprays were recorded using Mie-scattering, and plume-thimble (single plume spray) configurations were captured using DBI imaging. The full test matrix for these non-evaporative and non-reactive spray experiments and nozzle details is listed in Table 2.5.

In the second phase of the experiments, the investigation focused on single spray plumes generated using the thimble method. These sprays were tested under evaporative, non-reactive conditions. Simultaneous DBI and Schlieren imaging were employed to capture the characteristics of liquid-phase penetration and vapor-phase penetration behavior. The third phase of the experiments concentrated on reactive spray studies. In this stage, Schlieren imaging and natural luminosity measurements were conducted using a color high-speed camera to identify and distinguish the low-temperature ignition regions and high-temperature

Injector name	Orifice size (mm)	Normalized orifice size	Injection duration (ms)	Ambient densities (kg/m^3)	Injection pressures (bar)	Number of holes
A1	0.31	0.86	0.5	14.62, 27.69	1700, 2100	9
A2	0.31	0.86	0.35			
B	0.32	0.88	0.65			
C	0.365	1	0.728			

Table 2.5: Summary of injector specifications, including orifice size, injection duration, number of holes, and test conditions used for non-evaporative and non-reactive spray studies.

combustion zones within the spray. Injector-B was employed for both the second and third phases of the experimental campaign. To achieve the high temperatures and pressures re-

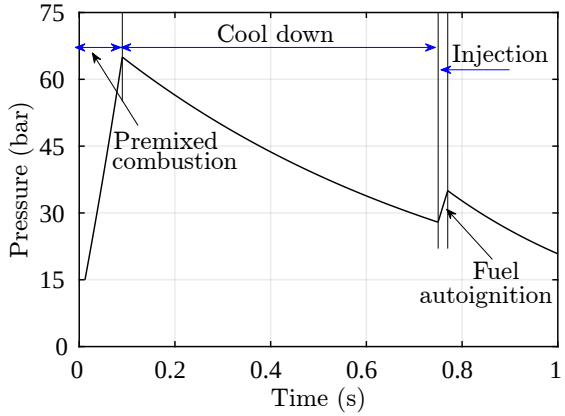

Figure 2.3: Schematic diagram of pre-mixed combustion (Dennis L. Siebers, 1998; Baert et al., 2009)

quired for studying evaporative and reactive sprays, a pre-mixed combustion process was employed in the OSCC, the process is shown in Fig.2.3. The process starts by evacuating the chamber with a vacuum pump to remove any residual gases. Following this, specific proportions of gases are introduced to form a lean fuel-air mixture, with the correct ratio established using partial pressures based on the desired volume percentages. Once the mixture reaches the target pressure/density, it is ignited using a spark plug, triggering a rapid rise in both pressure and temperature. After the peak conditions are reached, both pressure and temperature gradually decrease due to heat loss through the chamber walls. Once the temperature inside the chamber reaches the target value, the fuel is injected, where it subsequently undergoes auto-ignition. Temperature readings are taken from two sensors placed at opposite corners of the chamber, labeled as T_1 and T_2. The average temperature is then determined using the relation $T_{avg} = \frac{T_1+T_2}{2}$. In this study, hydrogen-air

Density (ρ_{amb}) (kg/m^3)	Target Temperature (K) ±50	H_2 (bar)	Air (bar)	N_2 (bar)	λ	$\%O_2$ after pre-mixed combustion
14.28	800	3.71	8.82	3.97	1	0
14.28	1000	3.71	8.82	3.97	1	0
27.24	800	6.65	15.84	8.77	1	0
27.24	1000	6.65	15.84	8.77	1	0

Table 2.6: Summary of target temperature and gas composition for evaporative sprays.

mixtures are used for premixed combustion with a stoichiometric fuel-to-air ratio ($\lambda = 1$). The objective is to achieve a final combustion product containing 0% oxygen, which allows for the investigation of non-reactive and evaporative spray behavior. The corresponding test conditions are listed in Table 2.6. The use of hydrogen ensures that no carbon dioxide is present in the combustion products. However, this results in a higher concentration of water vapor, which may condense on the chamber windows. To prevent this, the chamber walls are maintained at about 120°C and the metal walls are insulated. A specific oxygen concentration of 13% and 19% was used for the reactive spray studies. The corresponding test conditions are provided in Table 2.7. To reduce the intensity of pre-combustion, a controlled amount of excess nitrogen was added to the mixture. This addition lowers the reaction rate, as hydrogen (H_2) combustion at stoichiometric conditions ($\lambda = 1$) is highly energetic and can damage the combustion chamber windows.

Target density (kg/m^3)	Target temperature (K) ±50	H_2 (bar)	Air (bar)	O_2 (bar)	N_2 (bar)	λ	$\%O_2$ after combustion
14.38	850	1.8	13.71	1	0	3.2	19
	1150						
19.76	850	2.60	18.60	1.5	0	3	19, 13
	1150						
27.24	850	3.59	25.65	2	0	3	19
	1150						

Table 2.7: Summary of target temperature and gas composition for reactive sprays.

All initial phases of the experiments were conducted in Wärtsilä's Optical Spray Combustion Chamber (OSCC). In the fourth phase, the focus shifted to investigating near-field atomization behavior using ballistic imaging. These tests were conducted in a high-pressure, high-temperature constant-pressure flow (CPF) test rig at Chalmers University of Technology, capable of operating in both open-loop and closed-loop modes. For the present study, the chamber was used in a closed-loop configuration (no continuous flow) at ambient temperatures and various back and fuel injection pressures, effectively functioning as a

constant-volume vessel for capturing near-field breakup characteristics. Diesel was used for the near-field studies; fuel properties are listed in Table 2.4.

2.3 Strategies for isolating spray plumes

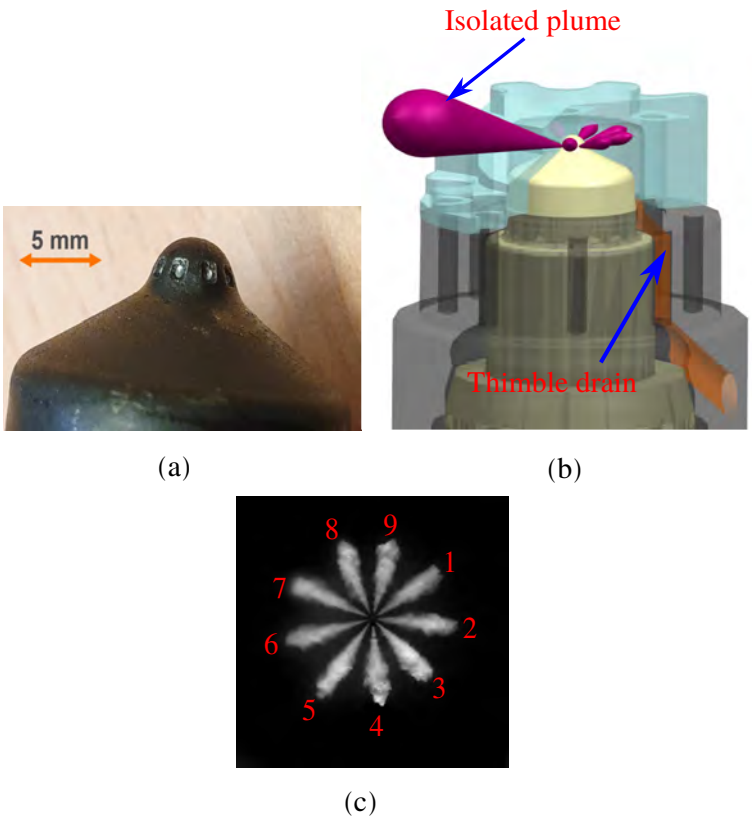

Figure 2.4: Spray plume isolation techniques: (a) nozzle with all holes sealed except one to isolate a spray plume (plume-blocking method); (b) CAD design of the thimble used to isolate a single spray plume (plume-thimble method); and (c) front view of the multi-hole (MH) injector spray showing plume numbering.

To study a single spray plume without interference from other plumes generated by the multi-hole nozzle (plume1-9), it is essential to isolate the plume. Two techniques were used for this purpose. The first technique involved sealing off all nozzle holes except the one in use, as illustrated in Fig. 2.4a, this approach is labeled plume-blocking. The second technique used a specially designed thimble attached to the nozzle (see Fig. 2.4b), which allowed only one spray plume—referred to as plume-thimble to enter the chamber, while the other plumes were collected and drained away. The injector was mounted at an angle near the bottom of the chamber, enabling the collected fuel to flow straight into the drain.

Additionally, the opening and closing of the thimble's drain valves were carefully timed after each injection to avoid pressure buildup in the drain system or thimble. For this study, the spray plume from the ninth nozzle hole was selected for injection using the thimble method, with the ninth plume (plume9) injected directly into the chamber and the remaining plumes collected by the thimble.

2.4 Optical methods

Various optical diagnostics have been utilized for both qualitative observation and quantitative measurement of spray characteristics. These non-intrusive diagnostics allow for detailed analysis without disturbing the spray dynamics. Optical methods for spray analysis are typically classified into imaging and non-imaging techniques. Imaging-based methods provide visual access to spray morphology and are employed to quantify parameters such as spray tip penetration, spray cone angle, and liquid core length. In contrast, non-imaging techniques are designed to extract statistical and dynamic properties of droplets, including size distributions, velocities, and number densities within the spray. A variety of these methods have been described in previous research, with each offering specific strengths and limitations depending on the parameter of interest and operating conditions. The previous section outlined key spray parameters commonly evaluated in spray diagnostics. The classification of experimental techniques according to the parameters they measure is summarized as follows. Liquid penetration was investigated using Mie-scattering and Diffuse back-Illumination (DBI) imaging. Vapor penetration was characterized using Schlieren imaging. For reactive sprays, natural luminosity imaging was employed, while near-field atomization was examined using ballistic imaging.

2.4.1 Diffuse back-illumination (DBI)

Diffuse Back-Illumination (DBI) is a light extinction measurement technique that compares the intensity of images taken with and without the spray present. The image without the spray serves as a reference, allowing calculation of the light attenuation caused by the spray. This makes the method self-calibrating and helps determine the optical thickness along the spray axis, which shows the spray structure and liquid phase boundaries. In the experimental setup, a continuous or pulsed light source is placed on one side of the spray chamber, and a high-speed camera is positioned directly opposite to record the transmitted light. A diffuser is used between the light source and the spray to provide uniform background illumination, and sometimes a Fresnel lens is added to increase background brightness. Because this method is less sensitive to small changes in the setup, it is frequently used for detecting liquid boundaries in both vaporizing and non-vaporizing sprays (Meijer et al., 2013; Raul Payri, Juan P. Viera, et al., 2017; Raul Payri, F. Salvador, et al., 2015; Jung et al., 2015). The captured images contain dark regions where the liquid phase blocks the light, bright regions where the light passes without obstruction, and gray regions that correspond to vapor. This contrast allows clear identification of the different spray phases. Figure. 2.5a illustrates the schematic layout of the DBI setup, and Fig. 2.5b shows the corresponding experimental photograph of the DBI system. In the present study, the DBI technique was employed to visualize liquid-phase penetration in both non-evaporative and

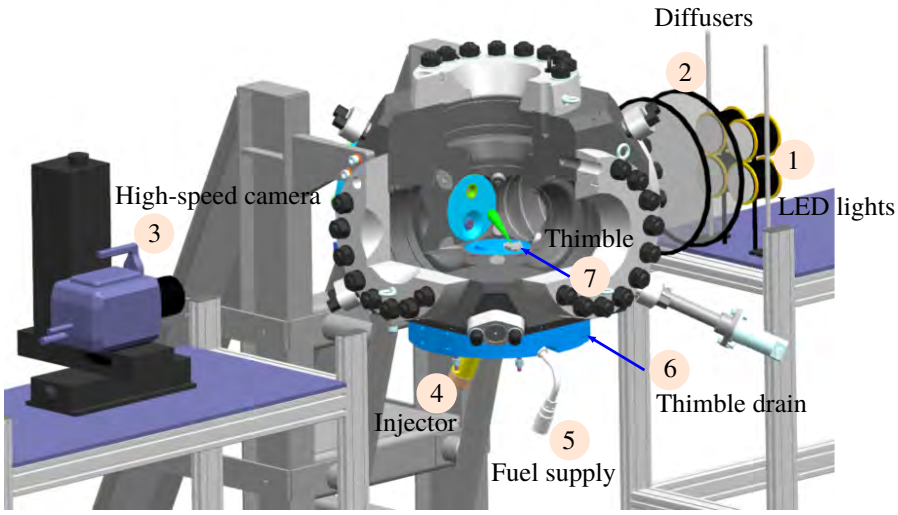

(a) Schematic diagram (CAD model) of DBI.

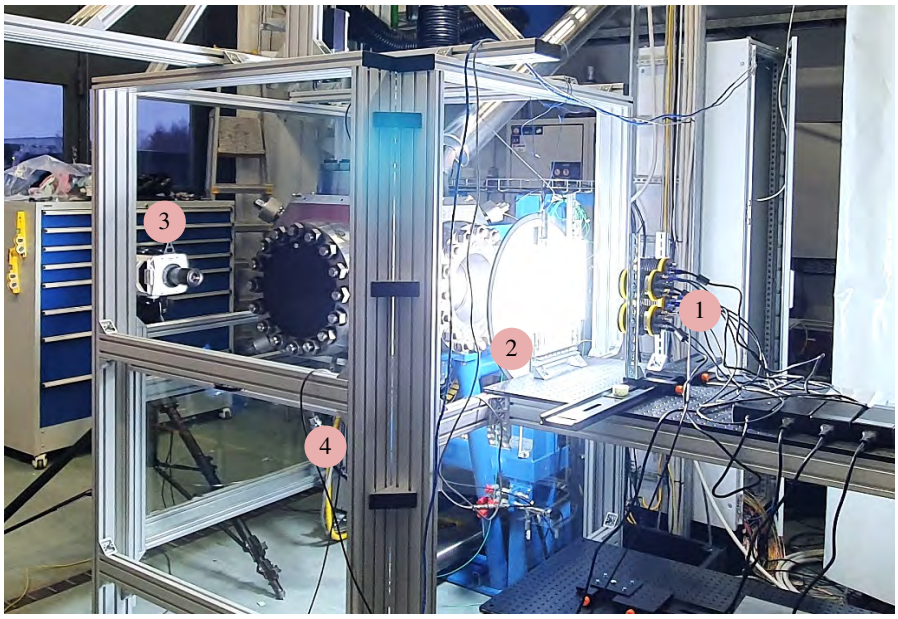

(b) Photograph of DBI experimental setup: (1) LED lights, (2) diffusers, (3) high-speed camera, and (4) injector and fuel supply module.

Figure 2.5: Diffuese back-illumination (DBI) experimental setup.

evaporative sprays under non-reactive conditions for single spary plume studies. A CMOS high-speed camera and an LED light source (Constellation 120E, Veritas) were mounted on opposite sides of the chamber and synchronized to capture images simultaneously.

2.4.2 Mie-scattering

Mie-scattering is another widely used method for imaging the liquid phase of sprays.(Kook and Lyle M Pickett, 2012). This technique relies on collecting light scattered by droplets at specific angles relative to the incoming illumination. The scattering process includes reflection, refraction, and diffraction effects. In spray diagnostics, a light source is directed onto the spray, and the scattered light originating exclusively from liquid droplets is recorded by a high-speed camera. Here, Mie-scattering is applied to visualize a multi-plume spray

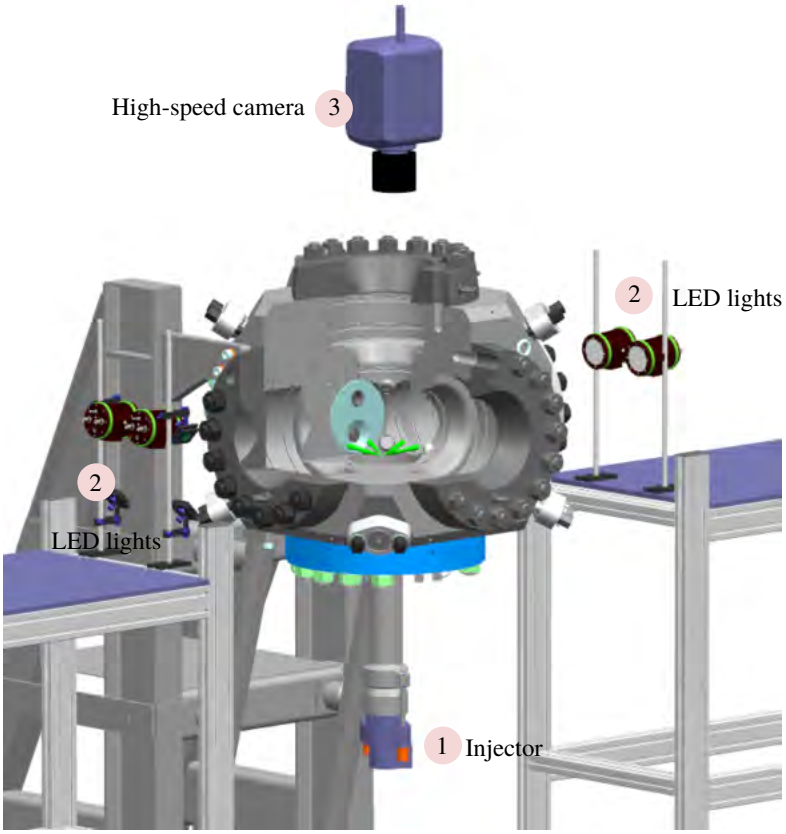

Figure 2.6: Schematic diagram (CAD model) of the Mie-scattering experimental setup.

under non-evaporative and non-reactive conditions. Figure. 2.6 illustrates the schematic layout of the Mie-scattering setup, and Fig. 2.7 shows the corresponding experimental photograph of the Mie-scattering system. LED lights are mounted on both sides of the spray chamber to provide uniform volumetric illumination of the spray plumes during Mie-

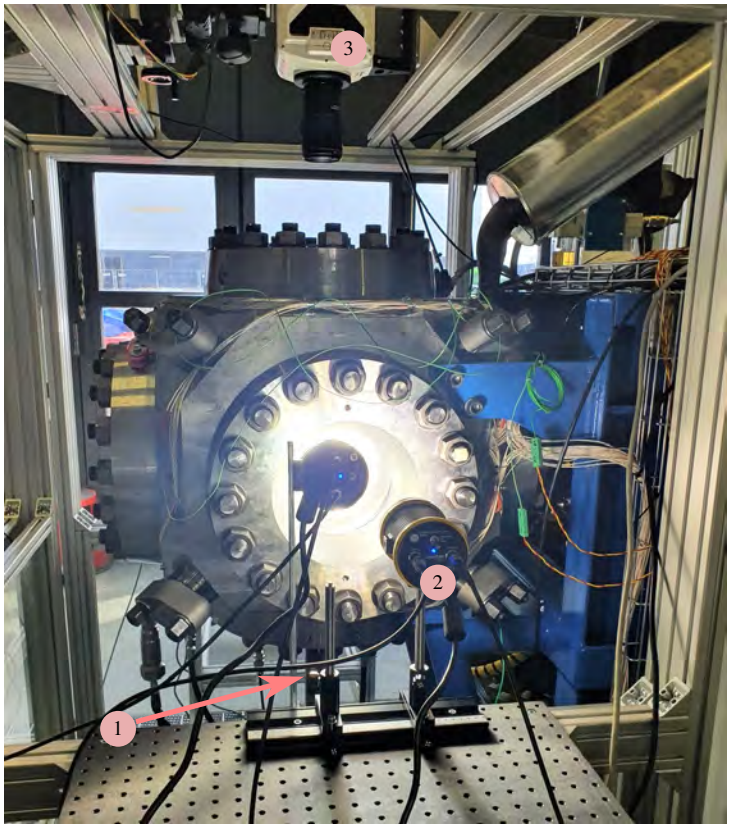

Figure 2.7: Photograph of Mie-scattering experimental setup: (1) injector and fuel supply module, (2) LED lights, and (3) high-speed camera.

scattering. As depicted in Fig. 2.6, the injector is positioned vertically at the bottom of the chamber, while the images are captured along the vertical axis from the top.

2.4.3 Combined Schlieren and Diffuse back-illumination (DBI)

Schlieren techniques are widely employed to visualize regions within a medium where refractive index gradients exist. When a collimated light beam passes through such a medium, some rays remain undisturbed, forming a uniform background in the image, while others are deflected, creating regions of varying brightness depending on the nature and direction of the deflection (Settles, 2001). In spray studies, these techniques are particularly effective in detecting vapor boundaries, as differences in refractive index exist between the vaporized fuel and the surrounding ambient gas. To investigate the simultaneous evolution of both vapor and liquid phases of a single spray under transient conditions, a combined diffuse back-illumination (DBI) and Schlieren imaging technique was implemented, allowing concurrent visualization of the spray's liquid and vapor regions across a range of chamber densities

and temperatures. The experimental setup, illustrated in Fig. 2.8, integrates both DBI and Schlieren imaging to capture the same injection event using complementary approaches. In the DBI system, light from a white LED source (400–700 nm) first passes through a diffuser to produce uniform illumination and then interacts with dichroic mirrors having a 600 nm cut-off edge. After traversing the spray, the light is reflected by a second dichroic mirror toward the first high-speed camera, enabling clear imaging of the liquid phase. Simulta-

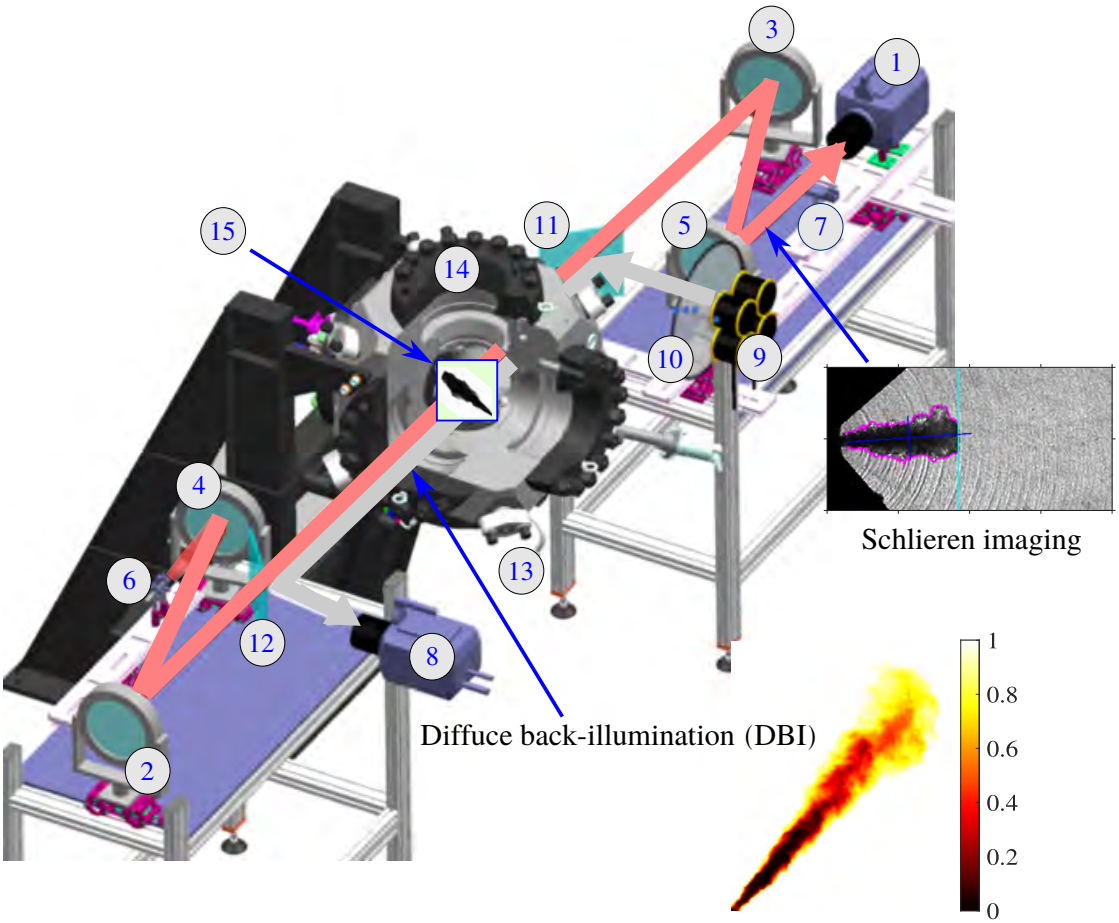

Figure 2.8: Experimental setup for simultaneous diffuse back-illumination (DBI) and Schlieren imaging: (1) high-speed camera (Schlieren), (2) parabolic mirror-1, (3) parabolic mirror-2, (4) plane mirror-1, (5) plane mirror-2, (6) laser, (7) knife edge, (8) high-speed camera (DBI), (9) LED lights, (10) diffuser, (11) dichroic mirror-1, (12) dichroic mirror-2, (13) injector, (14) spray measurement area, and (15) Optical Spray Combustion Chamber (OSCC).

neously, the Schlieren system employs a high-speed fiber laser (640 nm ± 10 nm) along with plain and parabolic mirrors, where the laser light bypasses the dichroic mirrors and is captured by a second high-speed camera to record the vapor phase. To prevent interference

from the LED illumination, a 650 nm band-pass filter is installed in front of the Schlieren camera. Both cameras are synchronized, ensuring that the DBI system records the liquid penetration at the same time as the Schlieren system captures vapor propagation, thereby providing a complete depiction of spray development. A 105 mm focal length lens with an f/2.8 aperture is used for both systems, and images are acquired at 29,000 frames per second with a resolution of 512×512 pixels and an exposure time of 9 μs, offering high temporal and spatial fidelity for accurately measuring both liquid and vapor phases.

2.4.4 Ballistic imaging

Ballistic imaging is an advanced optical technique designed to visualize dense fields with high spatial resolution. It captures photons that pass through the spray with minimal scattering, known as ballistic photons, enabling clear visualization of liquid structures within sprays of high optical depth (OD), typically greater than 5, where conventional imaging methods often fail (M. A. Linne et al., 2009). The fundamental principle of ballistic imaging involves separating these ballistic photons from multiply scattered photons using ultrafast optical gating. When a pulsed laser beam passes through a dense spray, most photons scatter multiple times due to the high droplet concentration, which leads to blurred and low-contrast images. However, a small fraction of photons pass straight through or experi-

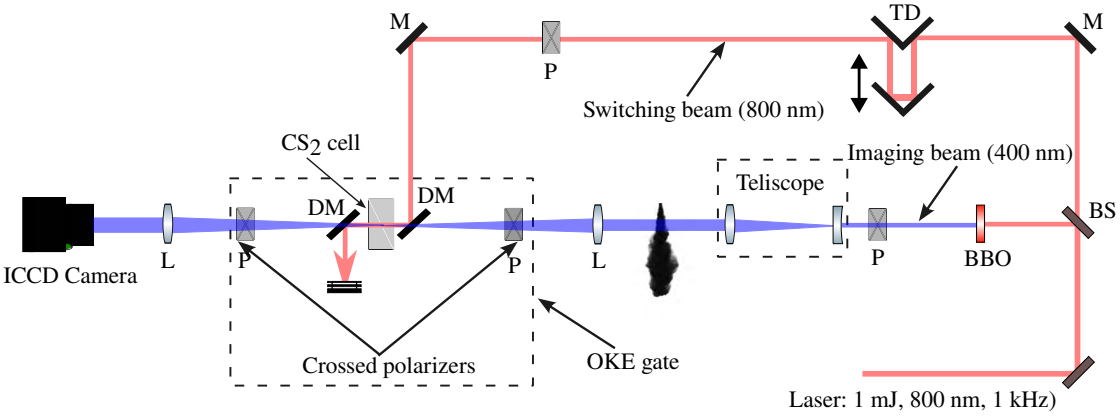

Figure 2.9: Schematic diagram of ballistic imaging. M: 800 nm mirror, DM: Dichroic mirror, TD: Time delay stage, BS: Beam splitter, BBO: Barium borate crystal, P: Polarizer.

ence minimal scattering; these ballistic photons retain sharp structural information about the spray. By employing an optical Kerr effect (OKE) gate (ultrafast shutter), only photons arriving within a few picoseconds, corresponding to the ballistic photons, are permitted to reach the detector. This effectively filters out the delayed, multiply scattered photons and produces sharp, high-contrast images of the liquid structures embedded within the spray. The ballistic imaging setup typically uses a femtosecond laser source generating short pulses at near-infrared wavelengths (e.g., 800 nm). The imaging beam is aligned collinearly with a switching pulse that activates the OKE gate, composed of two crossed polarizers and a birefringent medium. The switching pulse temporarily induces birefringence, allowing only

the earliest arriving photons to pass through the second polarizer. This gating window is extremely brief, usually lasting 1–2 picoseconds, which is crucial for isolating ballistic photons from slower, multiply scattered light. This approach enables two-dimensional imaging of inherently three-dimensional spray structures, clearly revealing features such as liquid cores, ligaments, and large droplets that primarily refract rather than diffusely scatter light. Ballistic images often show sharp interfaces between liquid and gas phases, providing valuable insight into spray morphology, breakup dynamics, and overall spray behavior. While ballistic imaging delivers high-resolution snapshots of spray structure, it cannot continuously record the full injection event because it requires precise synchronization with pulsed lasers and gating. As a result, imaging is performed at selected time delays after injection, with

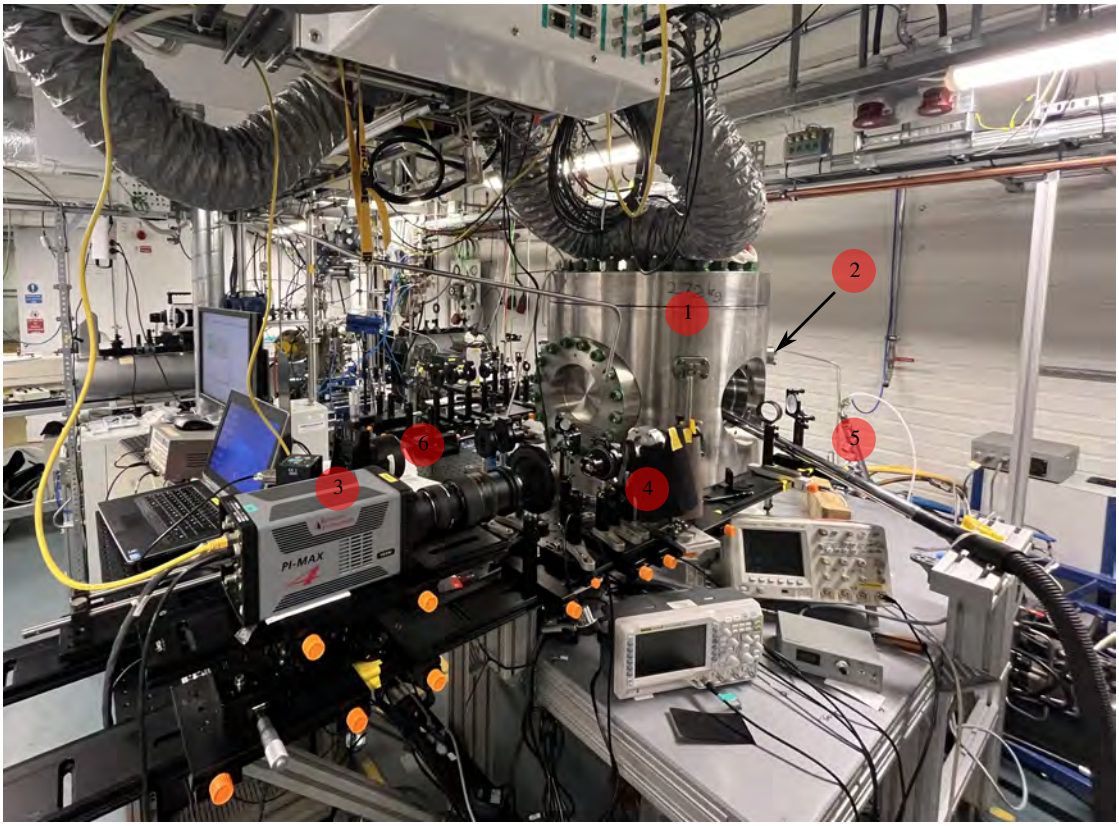

Figure 2.10: Ballistic imaging experimental setup: (1) spray visualization test rig, (2) fuel injector, (3) ICCD camera, (4) OKE gate, (5) fuel supply, (6) time delay stage.

multiple images collected at each interval to enable statistical analysis.

2.5 Image processing analysis of spray characteristics

This study used custom MATLAB code to perform image processing and contour detection on digital images. The initial processing steps were adapted to suit the specific type of image being analyzed, including Mie scattering, diffuse back-light, Schlieren, and ballistic images. These steps account for the unique visual features and contrast levels of each imaging method. However, once the spray boundary is identified, the following steps for measuring the spray characteristics are the same for all types of images. The next sections provide a detailed step-by-step explanation of the entire process.

2.5.1 Image analysis of non-evaporative and non-reactive sprays

Analysis of single-plume spray

The diffuse backlight imaging technique was used to visualize the single-plume spray. The post-processing of these images follows a procedure similar to that used for Mie-scattering images, with a few minor differences. The steps are as follows:

Step-Ia: As an initial step, background noise is typically removed from the spray image by subtracting the background image from the spray image. However, in this case, the spray image exhibits higher pixel intensities than the background due to the nature of the diffuse backlight imaging technique. Therefore, the spray image is subtracted from the background image to enhance the contrast between the spray and the background. To achieve this, a background image I_{bg} (Fig. 2.11a), captured without fuel injection, is used as a reference, and the spray image I_{spray} (Fig. 2.11b) is subtracted from it. The resulting image I_{sub} (Fig. 2.11c), which highlights the spray region while suppressing static background features, is computed as $I_{sub} = I_{bg} - I_{spray}$.

Step-Ib: The resulting image, I_{sub} (Fig. 2.11c) is then converted to binary format using Otsu's algorithm (Otsu, 1979), as illustrated in Fig. 2.11d. This adaptive threshold technique automatically determines an optimal threshold value to segment the spray region from the background, producing a binary image I_{binary} (Fig. 2.11d).

Step-Ic: After converting the image to binary, the single-plume spray is rotated to a vertical position to simplify the analysis and calculate the spray characteristics. The segmentation methods used are thoroughly detailed in the referenced studies (Shao et al., 2003; Delacourt et al., 2005; Rubio-Gómez et al., 2018). After binarization, the method for calculating spray characteristics proceeds as detailed in the following sections.

Step-Id: Spray penetration is usually measured by finding the axial distance between the nozzle outlet and the farthest point reached by the spray (R. Payri, J. Gimeno, et al., 2016; Xie et al., 2015). To keep the measurements consistent, the spray penetration length is defined as the distance from the spray tip along its axis to a line that contains 99% of the

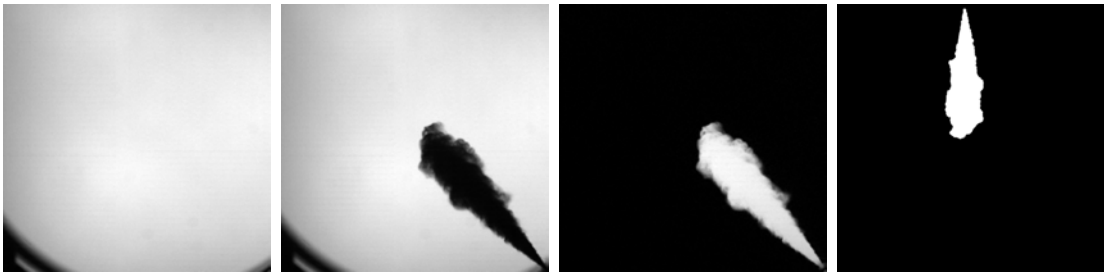

(a) I_{bg} **(b)** I_{spray} **(c)** I_{sub} **(d)** Binary image

Figure 2.11: Processing steps in backlight imaging of single-plume spray: (a) background image (I_{bg}), (b) spray image (I_{spray}), (c) subtracted image ($\text{I}_{\text{sub}} = \text{I}_{\text{bg}} - \text{I}_{\text{spray}}$), and (d) binary image after thresholding and rotation.

spray area, as shown in Fig. 3.14b. In the binary image, the spray area is found by counting all pixels with a value of one. Using the millimeter to pixel ratio, the spray penetration (in pixels) and spray area (in pixels squared) are converted to millimeters (Eqn. 2.1) and square millimeters (Eqn. 2.2). The formulas used are given below.

Spray penetration length (S):

$$\text{S(mm)} = \text{S(pixels)} \times \frac{\text{mm}}{\text{pixels}} \tag{2.1}$$

Area of spray (SA):

$$\text{SA(mm}^2\text{)} = \text{A(pixels}^2\text{)} \times \left(\frac{\text{mm}}{\text{pixels}}\right)^2 \tag{2.2}$$

The presence of a thimble obscures a section of the spray area near the nozzle tip, as depicted in Fig. 2.12. To account for this hidden portion, an equivalent spray area, $SA_{\text{equivalent}}$, is included alongside the measured area (calculated from Eq. 2.2). This adjustment leads to the following formula for the spray area when a thimble is used:

$$\text{SA}_{\text{plume-thimble}}(\text{mm}^2) = \text{SA}_{\text{measured}} + \text{SA}_{\text{equivalent}} \tag{2.3}$$

Spray cone angle (CA): A commonly used technique to determine the spray cone angle involves measuring the angle between two lines fitted along the edges of the spray boundary. These lines are identified using a least-squares fitting method and can be positioned either close to or at a distance from the nozzle tip. The length over which these lines are fitted typically depends on the spray penetration length or a multiple of the nozzle orifice diameter (D). In most cases, these lines are extended toward the nozzle tip coordinates, where they may either converge at a single point (the nozzle tip) or remain separate, depending on the spray structure and fitting method. The approach chosen to extend these fitted lines directly influences the resulting cone angle measurement. Therefore, it is essential to carefully select the fitting method, considering whether the lines are fixed at the nozzle tip

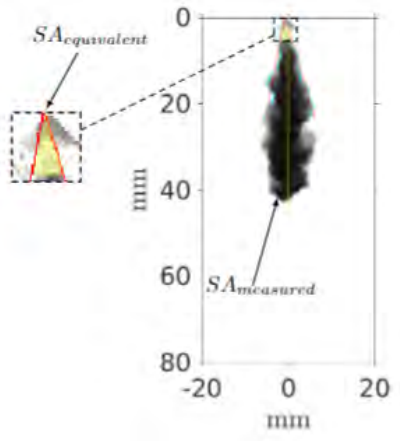

Figure 2.12: Spray area hidden by thimble thickness.

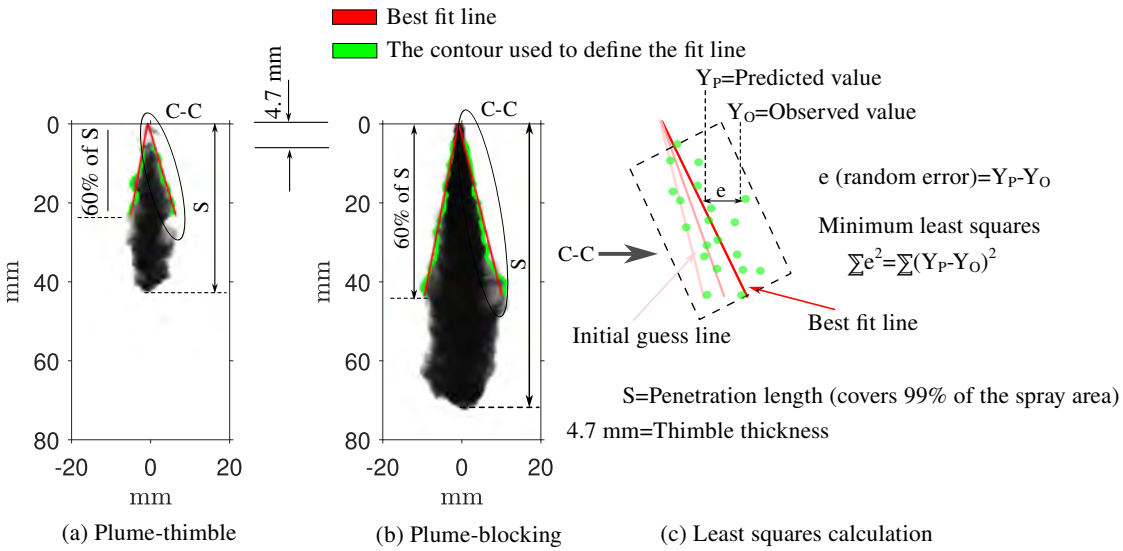

Figure 2.13: A schematic diagram for measuring spray penetration and cone angle.

coordinates or not, and the length over which they are fitted along the spray contour, as these factors critically affect the accuracy and consistency of the calculated cone angle. The first method calculates the cone angle by fitting lines along the spray contour and extending them to a distance proportional to the spray penetration length, typically about 60–70% of S (Delacourt et al., 2005; Payri et al., 2008; Rubio-Gómez et al., 2018). Alternatively, the penetration distance is often defined relative to the injector orifice diameter, ranging from 10D to 100D (Farrell et al., 1996; Shao et al., 2003; Dong et al., 2016). This involves using a least-squares fitting procedure to determine the best-fit lines, following a similar

principle to the triangle method introduced by Naber and Dennis L Siebers, 1996; F. Payri et al., 2014; Emberson et al., 2016; Suraj et al., 2021. Another approach calculates the cone angle by fitting lines between two selected points along the spray contour, without necessarily including the entire spray region, particularly near the nozzle tip. These points are carefully chosen to represent the specific area of interest within the spray pattern (R. Payri, J. Gimeno, et al., 2016; Ruiz-Rodriguez et al., 2019). In all these methods, the fitted lines may or may not intersect at the nozzle tip coordinates. This can introduce additional errors because the spray shape and boundaries change dynamically during transient conditions, and part of the spray is obscured by the thimble, making accurate boundary detection difficult in thimble.

In the present study, the first approach was modified to calculate the cone angle. Initially, the spray boundary was detected by binarizing the image, and an initial guess fitted line was drawn, anchored at the spray origin within the spray contour (Fig. 3.14bc). The line was then gradually shifted across one edge of the spray, calculated the least-squares error at each step. This process continued until the least-squares error reached its minimum, as shown in Fig. 3.14bc. The same procedure was applied to the opposite spray edge, and the angle between these two fitted lines was defined as the cone angle for that spray. Our experimental setup included a thimble that blocked the spray near the nozzle for up to 4.7 mm. Due to this obstruction, the spray boundary within the thimble could not be used for least-squares fitting. Instead, the spray contour from the thimble exit to 60% of the spray penetration length was used to compute the least-squares error. To maintain consistency and reduce variations in cone angle measurements caused by different methods, we excluded the spray region below 4.7 mm from the nozzle tip when calculating cone angles for plume-blocking and multi-plume sprays (plumes1–9). In all cases, the fitted lines were drawn from a fixed spray origin (Fig. 3.14b), located at the nozzle tip.

Analysis of multi-plume spray:

The Mie-scattering technique is utilized to visualize multiple sprays under ambient conditions, specifically under non-reactive and non-evaporative sprays. the image processing steps are described below.

Step-IIa The subtracted image (Fig. 2.14c) was then converted to a binary format using the Otsu thresholding algorithm (Otsu, 1979). The resulting binarized image is presented in Fig. 2.14d.

Step-IIb Initially, an image captured before injection was subtracted from the spray image to remove reflections and background noise. In the case of Mie-scattering, the background image (Fig. 2.14a) was subtracted from the original spray image (Fig. 2.14b), and the resulting image is shown in Fig. 2.14c.

Step-IIc A masking technique was subsequently applied to isolate individual spray plumes from the multi-spray image, following the approach described by Pastor et al., 2007; Macian et al., 2012; Raul Payri, Jaime Gimeno, Juan P Viera, et al., 2013. This process enabled the segmentation of the image into distinct regions, each corresponding to a single plume, allowing independent analysis of each spray structure. The result of this masking procedure is shown in Fig. 2.14e, which illustrates the appearance of plume-1 after masking. To

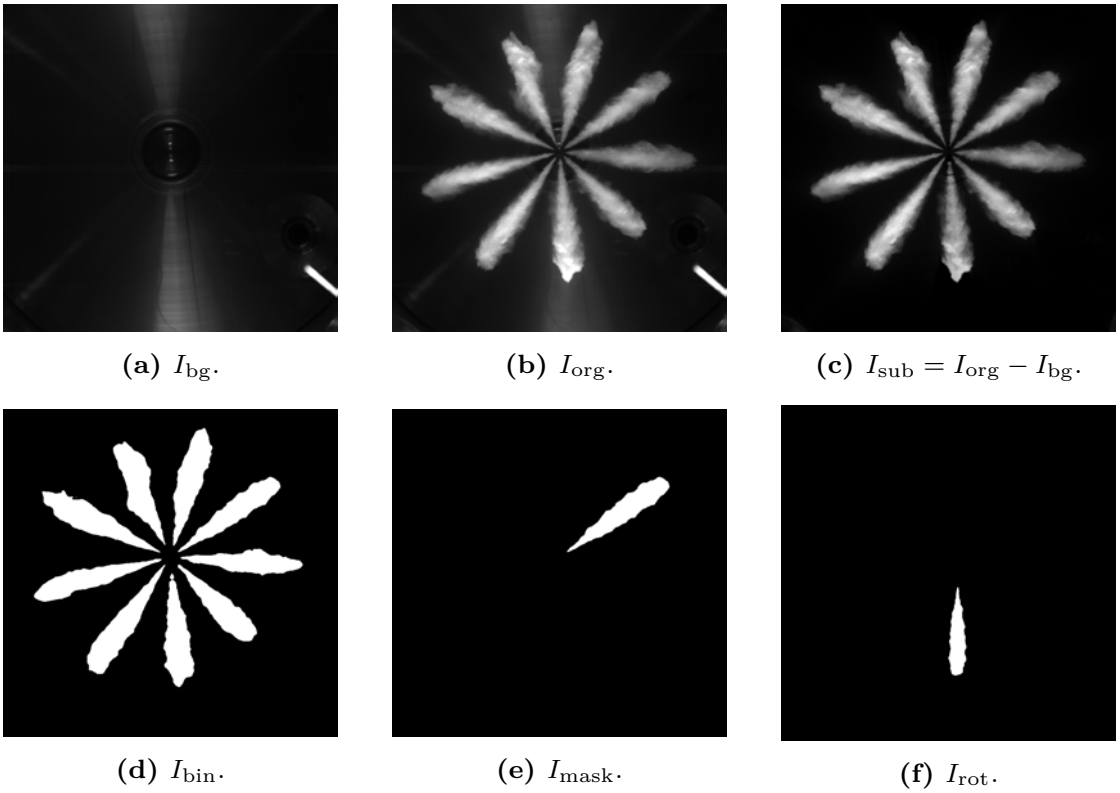

(a) I_{bg}. **(b)** I_{org}. **(c)** $I_{\mathrm{sub}} = I_{\mathrm{org}} - I_{\mathrm{bg}}$.

(d) I_{bin}. **(e)** I_{mask}. **(f)** I_{rot}.

Figure 2.14: Image processing sequence for spray image analysis: (a) background image, $\mathrm{I_{bg}}$; (b) original spray image, $\mathrm{I_{org}}$; (c) background-subtracted image, $\mathrm{I_{sub}} = \mathrm{I_{org}} - \mathrm{I_{bg}}$; (d) binarized image, $\mathrm{I_{bin}}$; (e) masked spray plume, $\mathrm{I_{mask}}$; and (f) rotated masked plume image, $\mathrm{I_{rot}}$.

facilitate further analysis and simplify the coding process, the central axis of each plume was measured relative to the horizontal axis. Then each plume was rotated to align vertically. An example of the rotated plume-1 is presented in Fig. 2.14f. This procedure was repeated for all spray plumes to ensure consistent orientation and enable uniform processing.

Step-IIc In the final stage of the image analysis process, key spray parameters such as penetration length, surface area, and cone angles were measured for each individual plume. A detailed explanation of the methods used to calculate these spray characteristics, similar to those applied in diffuse back-illumination, is provided in **Step-Id** (Section 2.5.1).

2.5.2 Image analysis of evaporative and non-reactive sprays:

Calculating different regions inside the spray:

In transient sprays, the liquid-phase structures lack sufficient time to evolve into a steady-state condition. As a result, the steady state liquid length typically observed in steady

or long-duration injections are not present. To investigate the behavior of such transient sprays, the spray field was divided into distinct regions based on variations in image intensity, as described in previous studies by Raul Payri, Juan P. Viera, et al., 2017; Pal and Bakshi, 2017; D. Ju et al., 2014. In diffuse back-illumination imaging, the presence of liquid

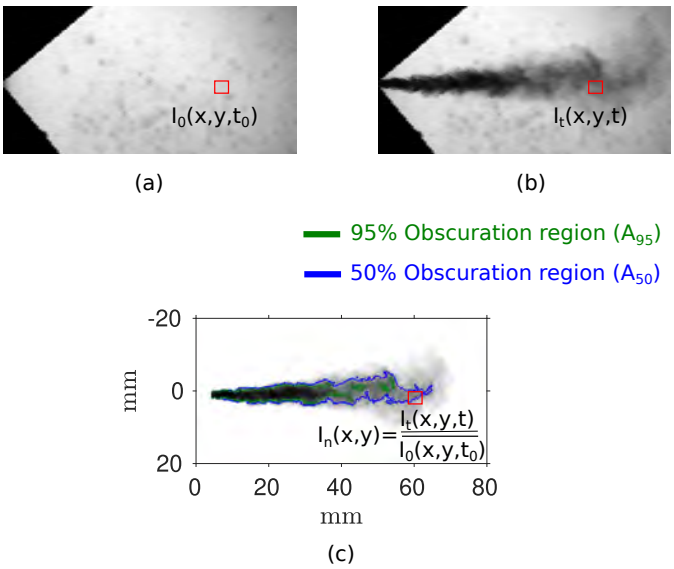

Figure 2.15: Segmentation of regions within an evaporating fuel spray.

droplets and vapor leads to scattering and absorption of background light. The degree to which light is blocked depends on the local concentration and distribution of these phases. To quantify this effect, each spray image was normalized by dividing its pixel intensities by those of a corresponding background image captured without the spray. This normalization process yields a relative transmittance map, which highlights spatial variations in light passage through the spray. Figure 2.15(a) presents the background image, (b) shows the spray at a specific time t, and (c) displays the normalized image. In this context, a normalized intensity of 0 indicates complete light blockage (100% obscuration), while a value of 1 indicates full light transmission (0% obscuration). These variations provide insight into the local density of the spray. The extent of light blockage is quantified using the optical depth, denoted by τ, which accounts for the combined effects of scattering and absorption. It is calculated using the Beer–Lambert law:

$$\tau = -\ln\left(\frac{I}{I_i}\right)$$

where I is the transmitted light intensity through the spray, and I_i is the incident light intensity in the absence of spray. The resulting optical depth map assigns each pixel a value representing the degree of light reduction at that location. To classify regions within the spray based on their opacity, threshold values of τ were applied. Two thresholds were selected: $\tau_{th} = 0.5$ and $\tau_{th} = 0.95$. Regions where $\tau > 0.5$ were considered moderately opaque, indicating that more than 50% of the incident light was blocked; the corresponding projected area is denoted as A_{50}. Regions where $\tau > 0.95$ were classified as highly opaque,

with less than 5% of the background light transmitted; these areas are labeled as A_{95}. This classification enables the identification and quantification of the densest regions within the spray, as illustrated in Fig. 2.15(c).

Measurement of vapor penetration length:

Schlieren imaging requires a tailored image processing approach that differs significantly from the methods used for diffuse back-illumination, especially when identifying the boundaries of evaporating fuel sprays. In Schlieren images, vaporizing sprays cause changes in the surrounding air's density and temperature, which appear as textured and non-uniform backgrounds, as shown in Fig. 2.16b. These background variations can obscure the spray structure, making it necessary to apply corrective processing techniques. To address this, a two-step procedure was implemented to reduce background interference and enhance the visibility of the spray. The first step involved normalizing each spray image ($\mathrm{I_{spray}}$) by dividing it by a reference background image. This reference was typically the frame captured immediately before the current spray image, denoted as $\mathrm{I_{n-1}}$, resulting in a normalized image defined as $\mathrm{I} = \mathrm{I_{spray}}/\mathrm{I_{n-1}}$. This method effectively reduces static background patterns under most conditions.

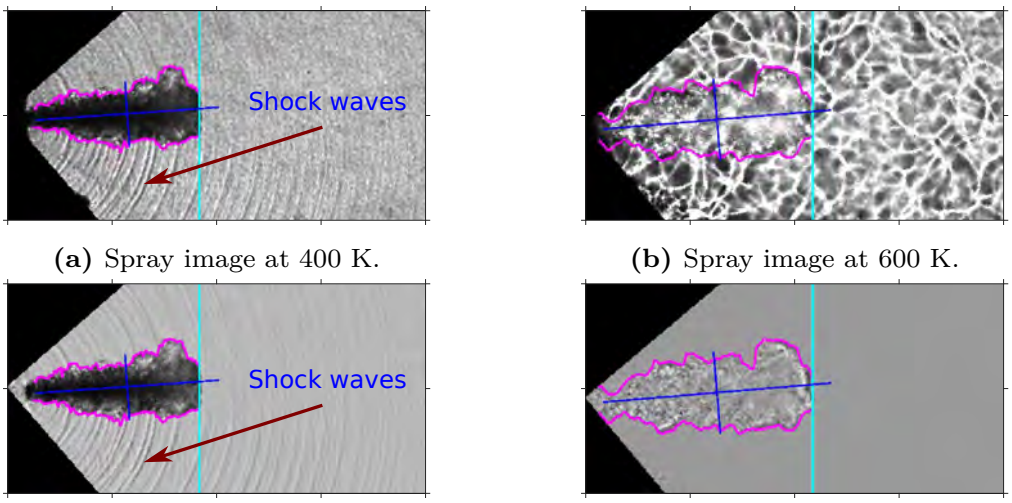

(a) Spray image at 400 K.

(b) Spray image at 600 K.

(c) Normalized image (I_{nor}) at 400 K.

(d) Normalized image (I_{nor}) at 600 K.

Figure 2.16: Schlieren imaging: A method for spray contour detection.

However, at elevated ambient temperatures such as 400 K, strong shock waves become visible in the Schlieren images. These shock waves move faster than the background structures and introduce additional noise when the previous frame is used as a reference (Figs. 2.16a and 2.16b). To minimize this issue, the first frame in the image sequence, captured before the spray and shock waves appear, was used as the reference. This approach helps isolate the spray features by reducing interference from dynamic flow structures. After background correction, a contrast enhancement step was applied to improve the visibility of low-intensity

regions within the spray. This was achieved by dynamically rescaling the pixel intensities using the transformation:

$$I_{nor} = \frac{I}{I + 0.96}$$

The constant 0.96 was selected based on empirical testing to ensure optimal contrast across the dataset. The resulting image (I_{nor}) provides a clearer and more consistent representation of the spray structure, as illustrated in Figs. 2.16c and 2.16d. To extract the spray boundaries from the normalized images, edge detection was performed using the Sobel operator (Gonzalez, 2009). This operator calculates the gradient of image intensity in both horizontal and vertical directions, highlighting regions with sharp intensity changes. The resulting gradient image was then converted into a binary edge map using Otsu's thresholding method (Otsu, 1979), which automatically selects an optimal threshold value based on image histogram analysis. To improve the continuity and visibility of the detected edges, a morphological dilation operation was applied. This operation used a structural element composed of horizontal and vertical lines to thicken the edges and connect any broken segments. Finally, any remaining gaps were filled, and the outermost contour of the spray was extracted as shown in Figs. 2.16 (a-d).

CHAPTER 3

Results and Discussions

This chapter provides a comprehensive discussion of the results obtained from the analysis of fuel spray characteristics under various operating conditions. The analysis is organized into five main categories based on the test conditions and specific objectives of the study. The first part of the discussion focuses on non-evaporative, non-reactive sprays, examining spray characteristics through isolated spray plumes and investigating plume-to-plume variations in multi-hole nozzle configurations. The second part addresses injector-to-injector variability, evaluating the influence of different injector designs on spray morphology and structural consistency under identical operating conditions. The third part discusses the behavior of evaporative, non-reactive sprays, with particular attention given to the development of liquid and vapor regions within the spray and the progression of vapor penetration length under elevated ambient temperatures. The fourth part extends the discussion to evaporative sprays operating under reacting conditions, focusing on flame development, combustion behavior, ignition characteristics, and the distinction between low-temperature and high-temperature combustion regimes for n-heptane sprays. The final part of the chapter examines the near-field atomization characteristics of fuel sprays. This section discusses primary breakup behavior and the early spray development process in the region immediately downstream of the nozzle exit, considering the effects of various fuel injection pressures and ambient back pressures on the spray evaluation process.

3.1 Results from non-evaporative and non-reactive sprays

3.1.1 Summary of paper-A: Shape/penetration analysis and comparisons of isolated spray plumes in a multi-hole Diesel spray

Dual fuel (DF) engines, commonly operating on liquefied natural gas (LNG) as the primary fuel, utilize a small quantity of liquid diesel as the pilot fuel to initiate combustion. The spray morphology of these pilot fuel sprays critically influences the ignition delay, flame propagation, combustion, and pollutant formation. Multi-hole nozzles are commonly employed in practical engines, so the spatial and temporal development of individual spray plumes from multi-hole diesel injectors affects local mixture formation and ignition development. The optical characterization of single plumes within a multi-plume spray is inherently challenging due to plume overlap, scattering interference, and complex internal nozzle flow phenomena. This paper addresses these challenges by systematically implementing two plume isolation techniques. The first involves using the thimble method to isolate a single

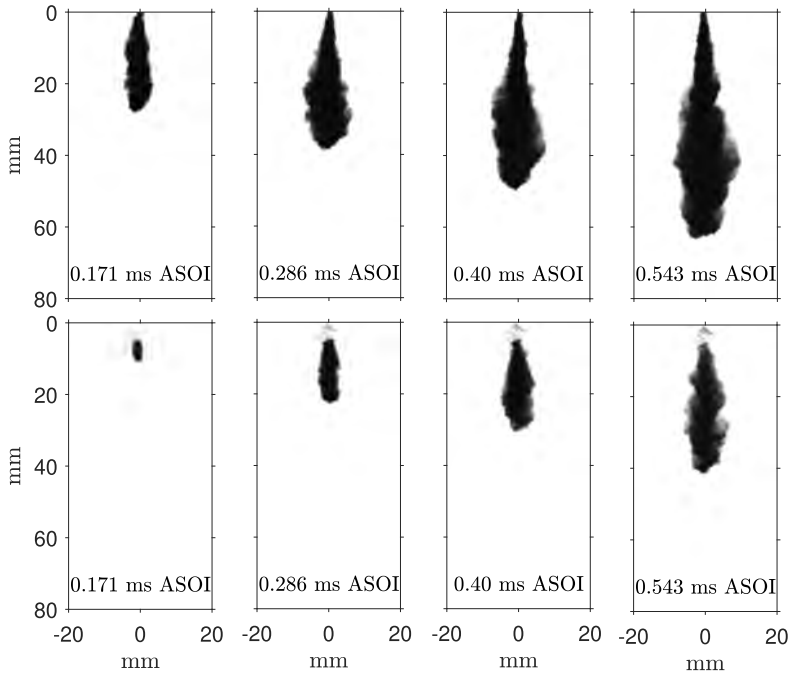

Figure 3.1: Image sequences of plume-blocking (first row) and plume-thimble (second row) at ρ_{amb}=14.62 kg/m^3, P_{inj} = 2100 bar.

spray from a multi-plume spray. The second technique modifies the nozzle by sealing all orifices except one to study a single spray. Finally, these two isolation methods are compared with the respective spray from a multi-plume spray, assessing their impact on the measured

spray characteristics under controlled, engine-relevant conditions. Fuel injection was tested in a constant volume spray chamber, allowing precise control of ambient conditions. To visualize sprays, Mie-scattering imaging was used for multi-plume sprays, while diffused back-illumination (DBI) was employed for single spray visualization under various ambient densities (ρ_{amb}: 14.62 kg/m^3 and 27.69 kg/m^3), injection pressures (P_{inj}: 1700–2100 bar), and an injection duration of 500 μs. The thimble method isolates a single plume externally

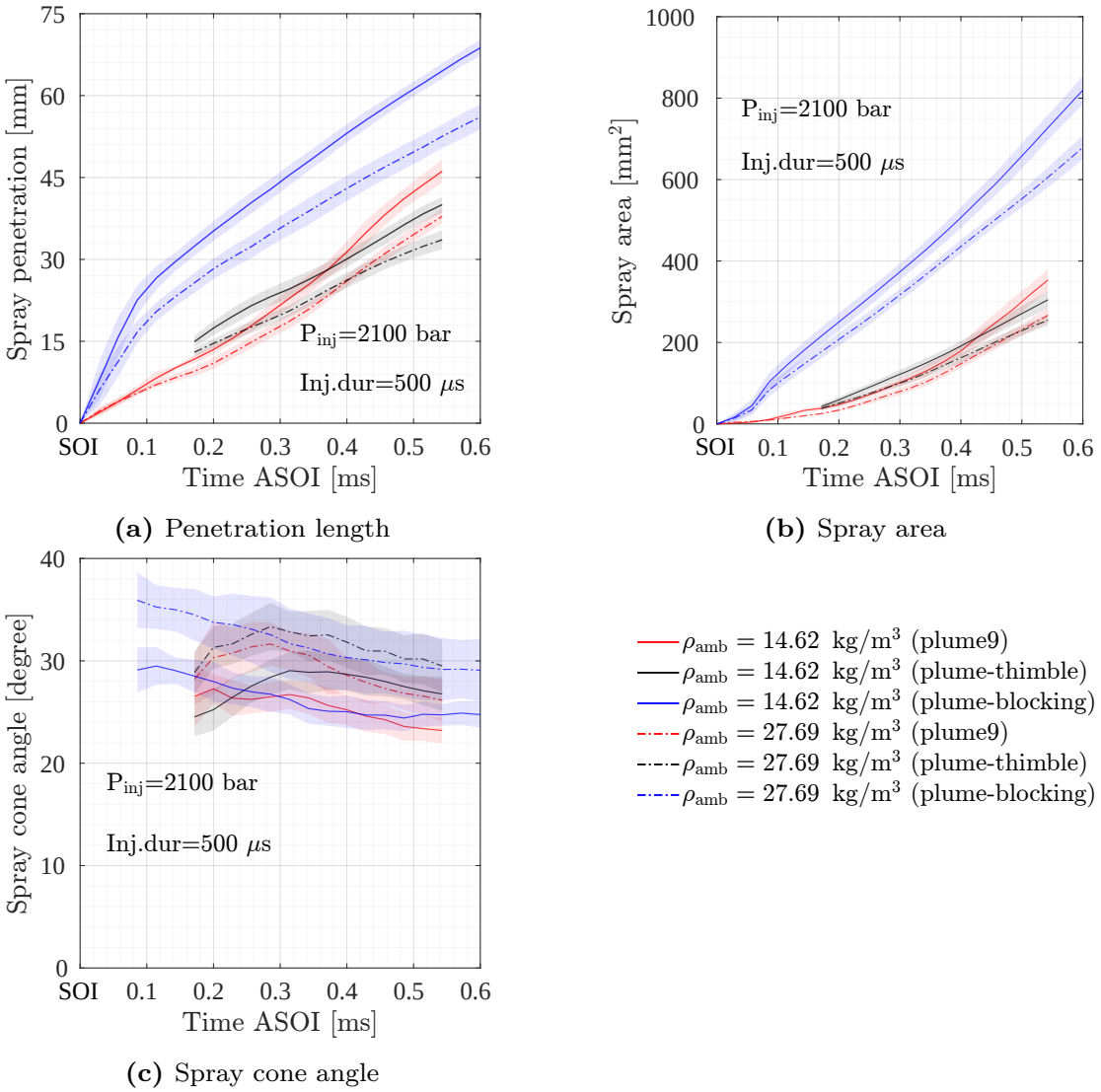

(a) Penetration length

(b) Spray area

(c) Spray cone angle

Figure 3.2: The effect of ambient density on spray characteristics: penetration length, spray area, and cone angle.

without altering the internal flow of the injector, while the plume-blocking method seals

selected orifices, forcing fuel through a single hole and thereby modifying the internal sac volume flow distribution. This distinction is crucial because any change in internal flow can significantly affect external spray characteristics.

Visualization results showed that the plume-blocking method led to longer spray penetration compared to the thimble method. This is clearly illustrated in Fig. 3.1, where the penetration lengths of the plume-blocked sprays exceed those of the thimble-isolated and standard multi-hole sprays under identical conditions. However, this increased penetration came at the cost of altered spray morphology, which deviated from the behaviour observed in the standard multi-hole configuration. This deviation was attributed to the redistribution of flow within the sac volume caused by sealing other orifices. Quite the opposite, the thimble method maintained the injector internal flow conditions, resulting in spray area and penetration lengths that precisely matched those of the unmodified multi-hole spray (plume9). This finding is directly supported by statistical data from Figs. 3.2a and 3.2b. These figures present average penetration and area plots that compare the spray penetration length and spray area of the plume-blocking and plume9 methods, clearly showing similar results. This evidence specifically indicates that the thimble method is more suitable for studying isolated plumes when the objective is to replicate the actual injector behaviour as accurately as possible.

3.1.2 Summary of paper-B: Impact of injector variability on transient spray characteristics in Diesel injectors

Differences in spray behaviour are commonly observed among diesel injectors, even when built to the same specifications. Slight differences in manufacturing tolerances and internal flow conditions within the injector typically cause these variations. As a result, it becomes challenging to accurately study the performance of individual spray plumes in multi-hole (MH) injectors, especially during transient injection events. Attempts to modify injectors to isolate specific plumes often increase these inconsistencies, which can affect the reliability of experimental results. In this work, the spray characteristics of four multi-hole diesel injectors with nearly identical designs were carefully examined and compared. Tests were conducted at injection pressures ranging from 1700 bar to 2100 bar, and at two ambient gas densities of 14.62 kg/m^3 and 27.69 kg/m^3. The behaviour of multi-plume spray symmetry and asymmetry patterns was studied to evaluate the consistency of each injector and to compare their spray characteristics. Furthermore, the single spray plumes (plume-thimble configuration) were compared across the injectors, with a specific focus on the individual spray pattern. To isolate and observe the individual plumes more precisely, a “thimble” method was utilised. The results show that even small differences between injectors can have a noticeable impact on transient spray behavior, even when the injectors share similar specifications.

The Root Mean Square Error (RMSE) is applied to evaluate the uncertainty and variability in spray penetration behavior across different injector plumes by systematically quantifying their deviations from an average reference profile. As a statistical measure, RMSE determines the extent of variation within a dataset. In this study, it is used to calculate how much the penetration length of each plume differs from a mean plume penetration curve, which is established by averaging the results from plumes 1 through 9. This makes

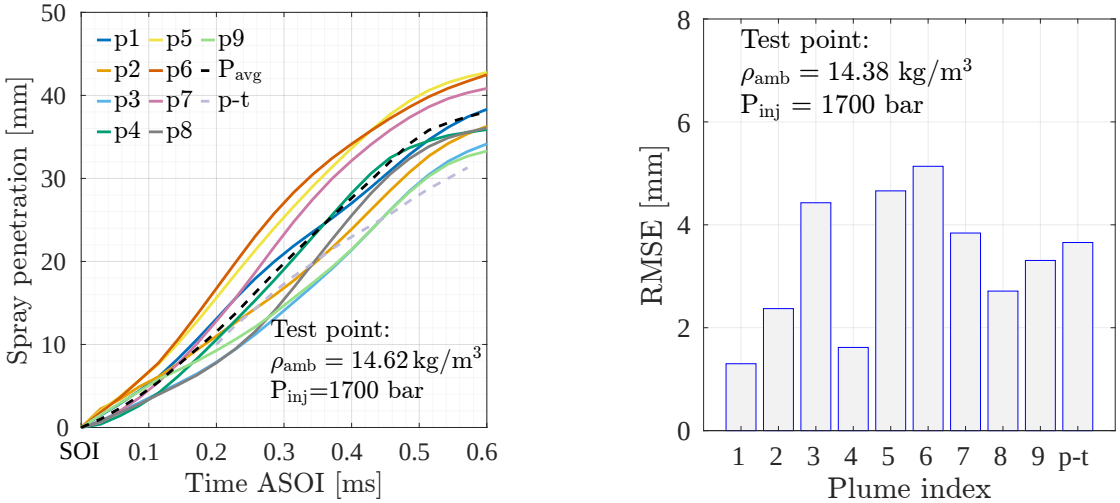

(a) Spray penetration. **(b)** RMSE.

Figure 3.3: (a) Comparison of penetration lengths for individual plumes ($P_i(t)$) and the averaged plume ($P_{avg}(t)$), shown as a thick black solid line, at the selected test condition. (b) RMSE values [mm] computed as a function of plume index using Eq. 3.1.

it possible to assess the consistency of individual plumes relative to the collective spray behavior, as shown in Fig. 3.3a. Among the evaluated plumes, it is observed that plume-9 exhibits a penetration profile closely matching that of the corresponding plume obtained using the thimble method.

The RMSE values for each plume (plumes 1–9 and plume-thimble) are determined using Eq. 3.1, where the mean penetration curve is based solely on plumes 1 to 9 to maintain consistency in comparison:

$$\text{RMSE}\,[\text{mm}] = \sqrt{\frac{1}{n}\sum_{t_1}^{t_2}\left(P_{avg}(t) - P_i(t)\right)^2} \tag{3.1}$$

In this formula, n represents the number of recorded data points, while t_1 and t_2 denote the start and end of injection, respectively. The term $P_{avg}(t)$ refers to the average penetration length at time t, obtained from plumes 1 to 9, whereas $P_i(t)$ indicates the penetration length of the i^{th} plume at the same time, with i ranging from 1 to 9 and including the thimble-based measurement (p-t). The computed RMSE values are presented in Fig. 3.3b, corresponding to an ambient density of $\rho_{amb} = 14.62\,\text{kg/m}^3$ and an injection pressure of $P_{inj} = 1700\,\text{bar}$. Higher RMSE values indicate greater deviation from the average plume behavior, while lower values reflect closer alignment with the mean profile. Additionally, when RMSE values remain relatively uniform across the plumes, it suggests a symmetric spray pattern, whereas significant variations imply asymmetry in the spray distribution. Upon detailed examination, distinct differences in injector behavior were observed.

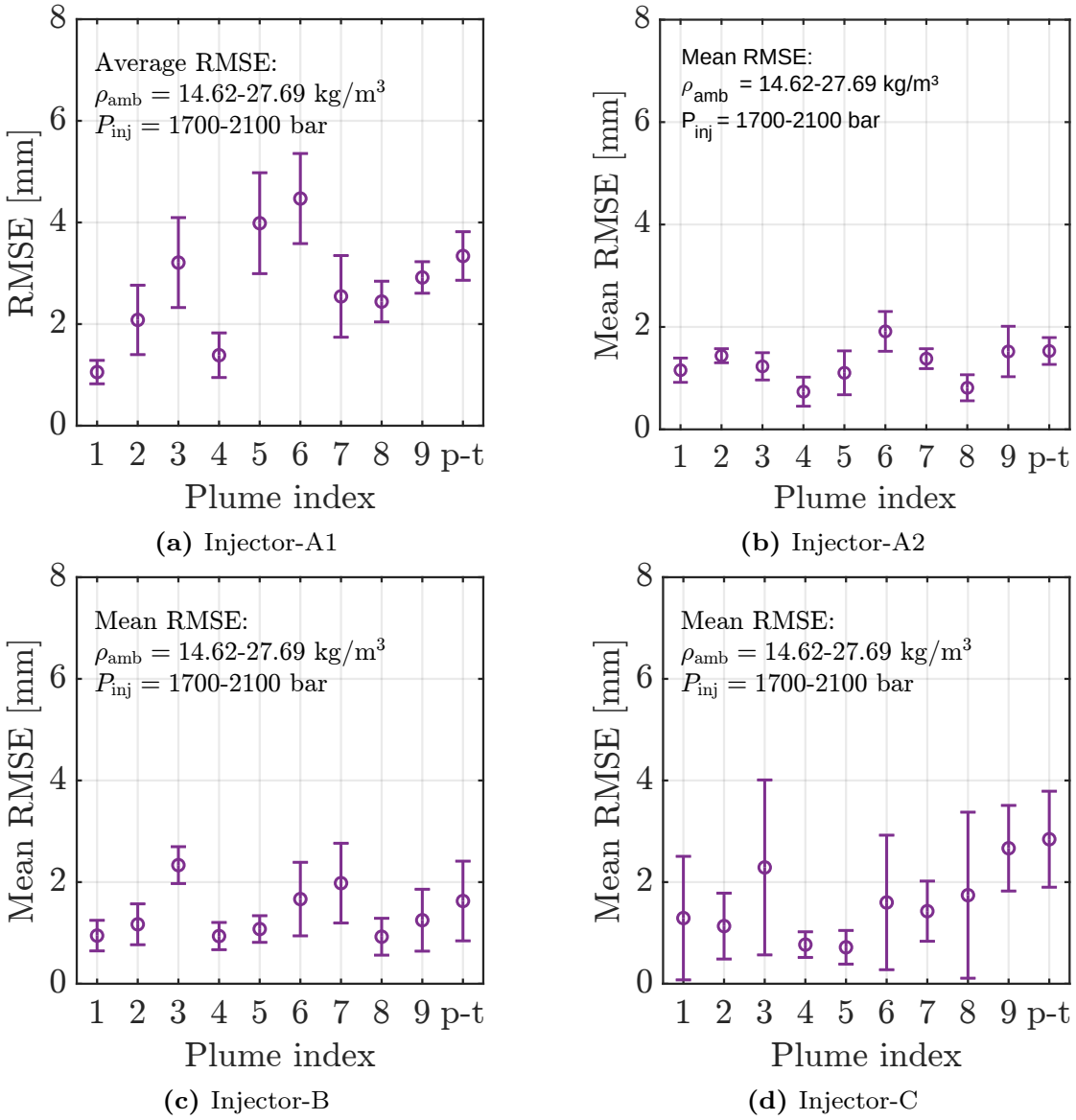

(a) Injector-A1 **(b)** Injector-A2

(c) Injector-B **(d)** Injector-C

Figure 3.4: The sum of RMSE values and their corresponding standard deviations were calculated for each plume across all operating conditions for all four injectors: A1, A2, B, and injector C.

Injectors A1 and A2—although manufactured by the same company and differing only in build numbers—exhibited significant variations in spray penetration lengths (Figs 3.4a and 3.4b). These discrepancies were attributed to minor deviations in orifice hole drilling and manufacturing tolerances, which led to uneven flow distribution around the injector needle [ref]. The analysis further revealed that spray behavior became highly unstable under transient operating conditions, particularly when the injector needle was partially open.

Under these conditions, injectors A2 and B produced relatively consistent spray patterns (Figs 3.4b and 3.4c), whereas injector C exhibited pronounced plume-to-plume irregularities (Fig. 3.4d). This instability complicates the prediction and modeling of fuel spray patterns during dynamic engine operation, where partial needle lifts disrupt uniform flow structures. The thimble method proved effective for isolating and analyzing individual spray plumes.

3.2 Results from evaporative and non-reactive sprays

3.2.1 Summary of paper-C: A transient mode pilot sprays for dual-fuel combustion

Pilot sprays tend to vaporise quickly due to short injection durations, especially under the high-pressure and high-temperature conditions typically found in engine operation. However, accurately measuring spray liquid penetration and area becomes challenging because of the injection's rapid evaporation and transient nature. If the spray does not vaporise completely, it may result in ignition delays or even misfires, affecting combustion stability and leading to higher emissions. Hence, understanding the behaviour of evaporative pilot sprays, particularly how ambient conditions like temperature and density influence spray characteristics, is important for optimising ignition timing, improving engine efficiency, and reducing emissions. Such information is also valuable for the development and validation

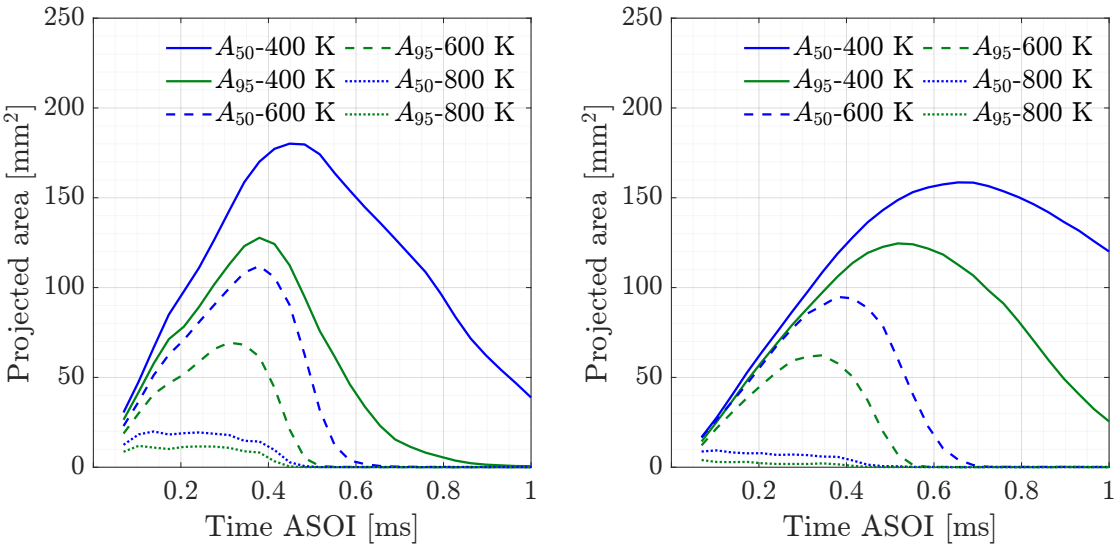

(a) Projected area at 14.28kg/m^3 **(b)** Projected area at 27.24 kg/m^3

Figure 3.5: Projected areas of the 50% and 95% obscuration regions as a function of time after start of injection at 2100 bar injection pressure.

of mathematical models for pilot spray combustion processes. This paper focuses on investigating the behavior of transient n-heptane pilot sprays under engine-relevant conditions using a constant-volume optical spray combustion chamber (CV-OSCC). Experiments were conducted across a range of ambient temperatures (400, 600, 800, and 1000 K, with an uncertainty of ±50 K), densities ρ_{amb} = 14.28 and 27.24 kg/m^3, and injection pressures of 1700 and 2100 bar. To avoid a reactive ambient, an inert ambient atmosphere was created using a pre-mixed combustion approach. Diffused back-illumination (DBI) and Schlieren imaging were used together to capture both the liquid length c and vapor penetration characteristics simultaneously.

The different regions of the spray are presented in Figs. 3.5a and 3.5b. These figures show the projected surface area of the liquid phase at injection pressures (P_{inj}) of 1700 bar and 2100 bar, and ambient densities of 14.28 kg/m^3 and 27.24 kg/m^3, respectively. The plots highlight how the projected area of the liquid phase changes over time within the 50% and 95% obscuration regions. This helps in comparing the evaporation behavior and liquid spray spread under different combinations of ambient density and temperature. The results

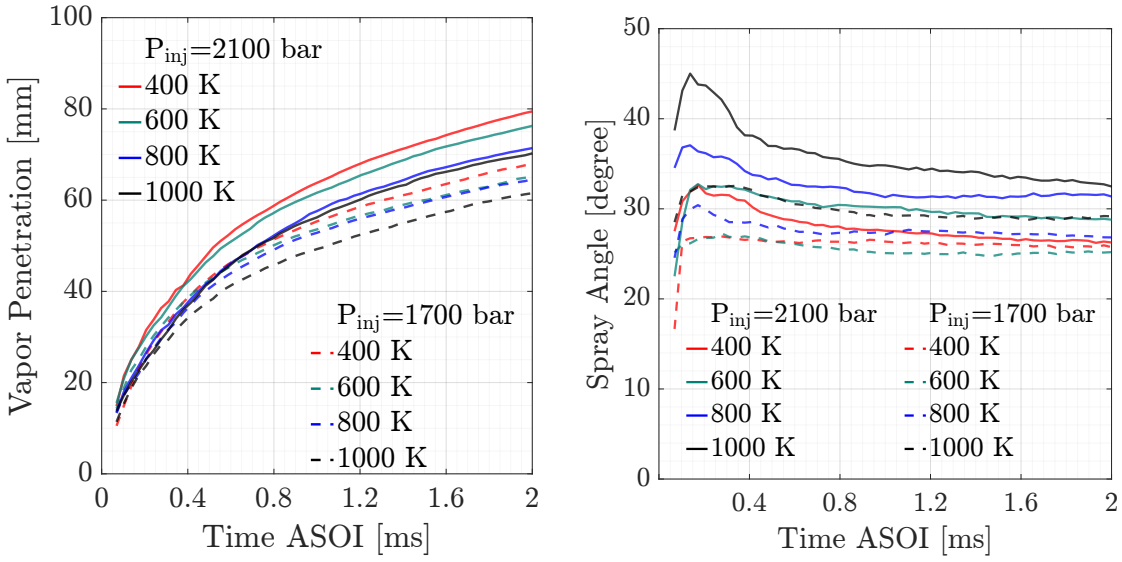

(a) Effect of temperature on vapor penetration length at 14.28 kg/m^3.

(b) Effect of temperature on cone angle at 14.28 kg/m^3.

Figure 3.6: Behavior of vapor penetration length and cone angle.

shown in Figs. 3.6 and 3.7 depict the variation in vapor penetration length and spray cone angle over time after the start of fuel injection. These observations demonstrate the impact of ambient density, injection pressure, and ambient temperature on spray characteristics, specifically at an ambient density of 14.38 kg/m^3. It is evident that the vapor penetration length decreases as the ambient density increases. This is primarily due to the higher aerodynamic drag exerted by the denser surrounding gas, which causes greater momentum loss and restricts the axial movement of the spray. On the other hand, an increase in injection pressure results in a narrower spray cone angle, owing to the higher velocity of the

fuel jet. Moreover, a rise in ambient temperature leads to a reduction in vapor penetration length and enhances the evaporation rate. Higher temperatures provide additional thermal energy, enabling quicker evaporation of fuel droplets. This promotes faster mixing with the surrounding air and limits the axial spread of the vapor phase. The Schlieren visualization images (Fig. 3.7) further confirm that the liquid phase in these pilot sprays is present only for a short distance and duration after injection.

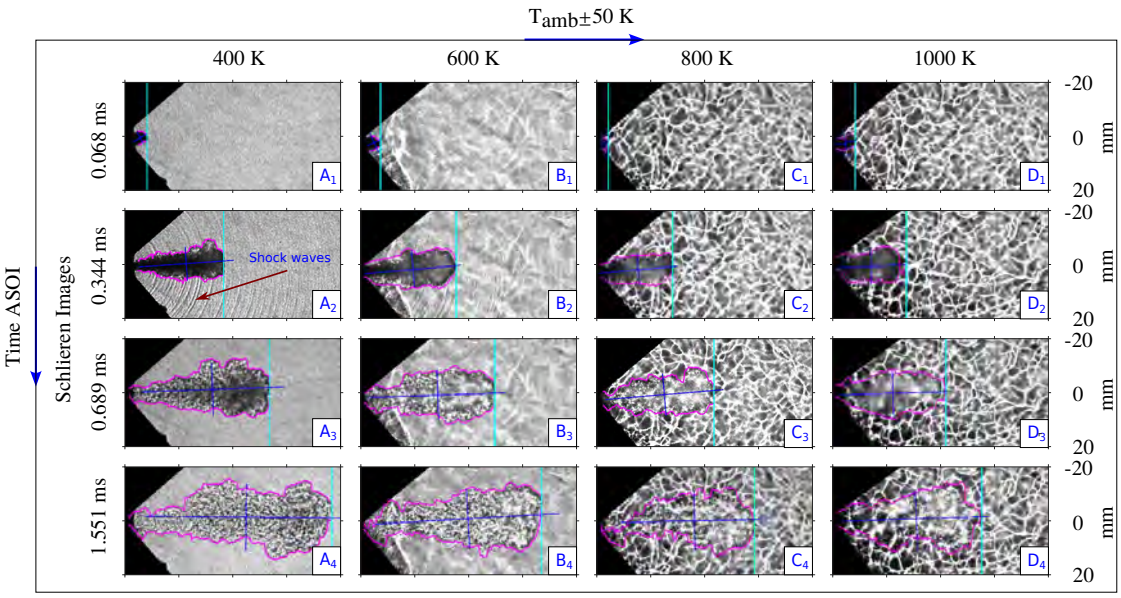

Figure 3.7: Schlieren imaging at $\rho_{\text{amb}} = 14.28$ kg/m^3 and $P_{\text{inj}} = 2100$ bar.

3.3 Results from reactive sprays

3.3.1 Summary of paper-D: Influence of ambient pressure, temperature, and injection pressure on reactive pilot n-heptane spray evolution using optical imaging

An experimental investigation was carried out to study n-heptane spray combustion in a constant-volume chamber under engine relevant thermodynamic and injection conditions. The ambient densities were set at 14.38, 19.76, and 27.24 kg/m^3, injection pressures at 1700 bar and 2100 bar, and ambient temperatures at 1150 K (±50 K) and 850 K (±50 K). Post-premixed combustion oxygen concentrations of 19% and 13% were examined to evaluate the influence of oxygen availability on combustion behavior. Spray combustion is a complex process that includes atomization of liquid fuel, evaporation of droplets, mixing of fuel with air, followed by ignition and combustion. Studying these interconnected processes under different ambient densities and temperature conditions is important for improving combustion efficiency and for controlling emissions in systems like diesel engines and gas

turbines. In this study, two optical diagnostics such as natural luminosity and Schlieren imaging methods were employed to investigate *n*-heptane spray behavior under reactive conditions under various ambient conditions.

Natural luminosity imaging records the visible light emitted from the spray flame during combustion, originating from both chemiluminescence of reactive species and thermal radiation from soot particles. The color and intensity of this emission provide qualitative information about the combustion regime and dominant reaction processes. At an ambient temperature of 850 K, the color camera captured a noticeable blue flame (Fig. 3.8), which is typically attributed to the chemiluminescence of radicals such as CH^*, C_2^*, and OH^*. The presence of this faint blue emission indicates the onset of low-temperature combustion (LTC), also referred to as the cool-flame regime, where low-temperature oxidation (LTO) reactions dominate before the main ignition event. At this stage, the fuel has largely vaporized and mixed with the surrounding air, and ignition occurs primarily in the vapor phase through kinetically controlled oxidation. The limited heat release results in a short-lived, transparent, and soot-free flame. These observations are aligned with the Schlieren images acquired under the same thermal conditions, as shown in Fig. 3.9. In Fig. 3.8,

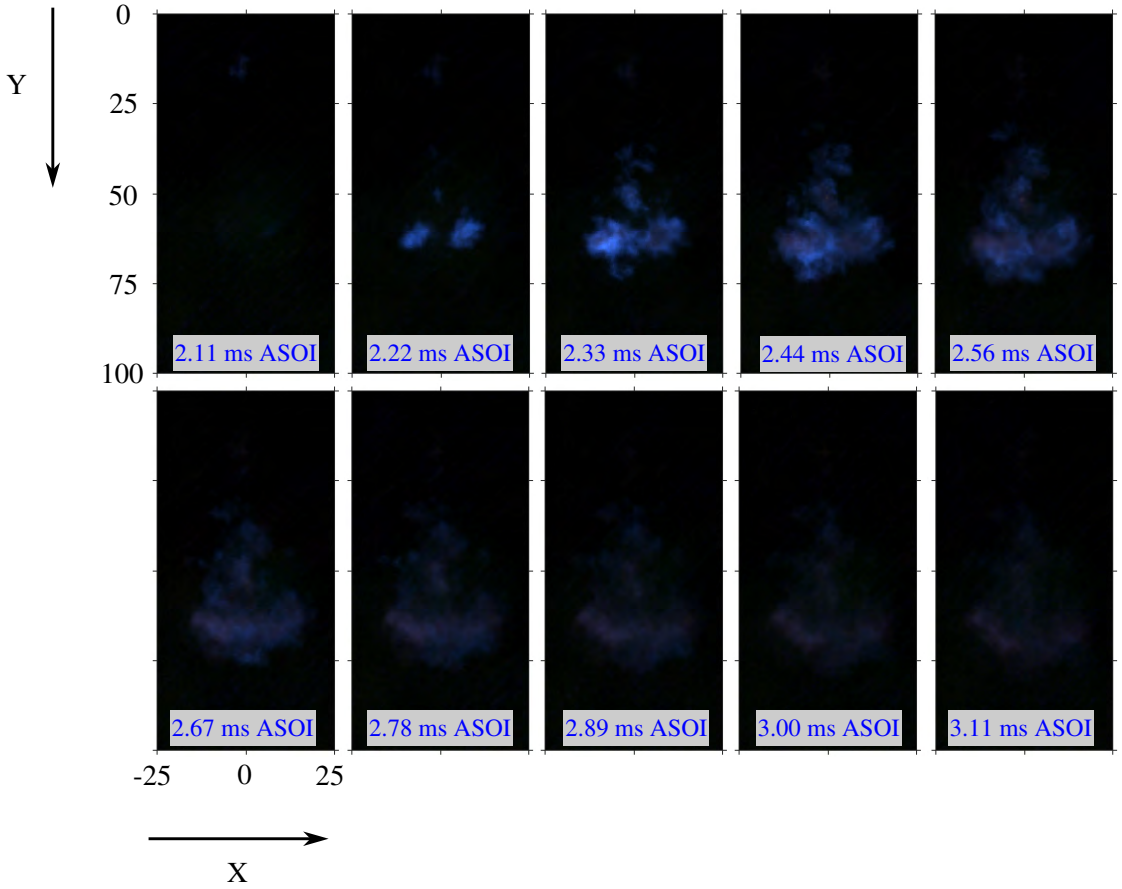

Figure 3.8: Natural luminosity flame images at 850 K, ambient density 14.38 kg/m^3, injection pressure 2100 bar.

the natural luminosity image at 850 K shows a distinct compact blue flame of the spray, highlighting localized reaction zones where the fuel and oxidizer are well mixed. The corresponding Schlieren image in Fig. 3.9 (1.52-1.86 ms ASOI) illustrates that, as the blue flame develops, the visible spray structure begins to fade. This reduction in Schlieren contrast occurs due to refractive index matching between the fully vaporized fuel–air mixture and the surrounding hot gas, making the vapor optically homogeneous relative to the background. The liquid spray disappears at the same time the blue flame forms, which shows that vaporization happens before ignition and that the combustion takes place in the gas phase during the low-temperature combustion (LTC) or cool-flame stage. As the ambient

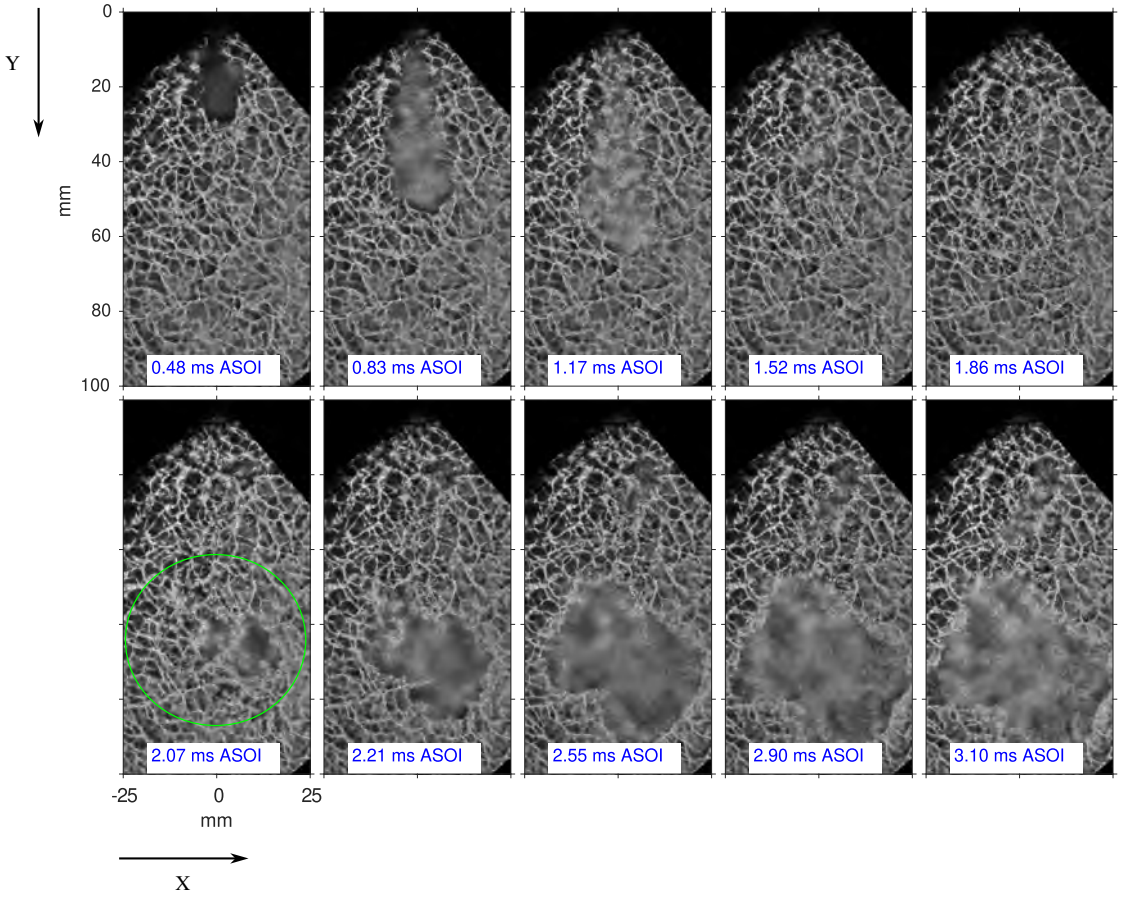

Figure 3.9: Schlieren flame images at 850 K, ambient density 14.38 kg/m^3, injection pressure 2100 bar.

temperature increases beyond 1000 K, the flame characteristics change considerably. At 1150 K, the natural luminosity images exhibit a bright yellow flame without any visible blue flame as Shown in Fig. 3.10. The yellow emission arises from blackbody radiation of incandescent soot particles formed in locally fuel-rich regions where the mixing process is incomplete. This condition represents the high-temperature combustion (HTC) regime, dominated by diffusion-controlled burning and strong radiative heat release. The absence

of blue chemiluminescence indicates that the low-temperature oxidation stage is effectively suppressed at this elevated temperature. The luminous yellow flame develops much earlier after injection, reflecting a shorter ignition delay (Figs. 3.12a and 3.13a), enhanced evaporation, and more intense heat release under high-temperature conditions. In Fig. 3.10

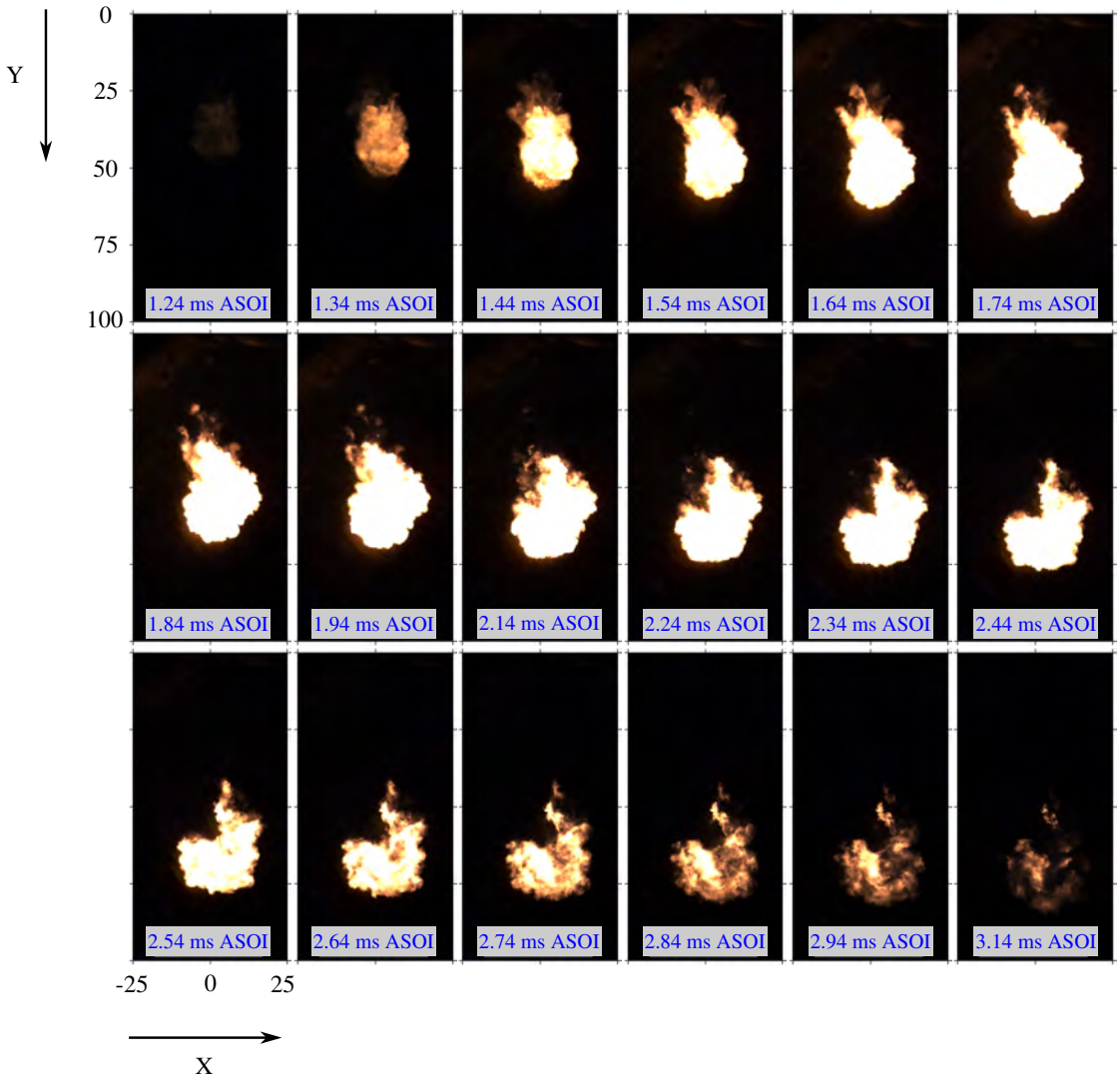

Figure 3.10: Natural luminosity flame images at 1150 K, ambient density 14.38 kg/m^3, injection pressure 2100 bar.

(1.34-3.14 ms ASOI), the natural luminosity image at 1150 K shows a continuous yellow flame along the spray axis, indicating significant soot formation and diffusion-controlled combustion. The flame occurs in the region where the fuel vapor mixes with air and reacts, showing that high-temperature oxidation dominates the process. The corresponding Schlieren image in Fig. 3.11 (1.17-2.55 ms ASOI) displays strong refractive index gradients

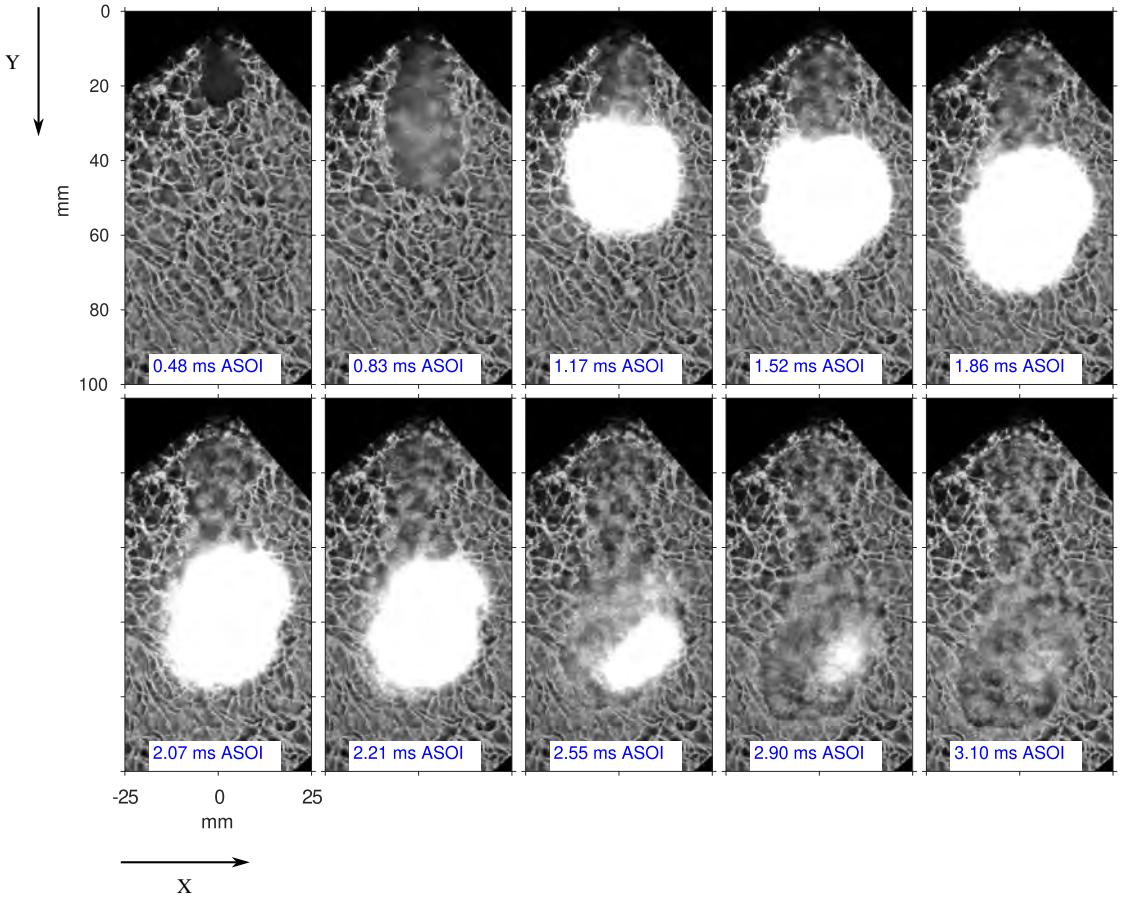

Figure 3.11: Schlieren flame images at 1150 K, ambient density 14.38 kg/m^3, injection pressure 2100 bar.

along the spray, highlighting regions of intense heat release and high-temperature reactions. Unlike the 850 K case, the Schlieren signal remains strong throughout the combustion, clearly marking the main flame front and the regions of active reaction. These observations confirm the transition from low-temperature, kinetically controlled reactions at 850 K to high-temperature, diffusion-controlled combustion at 1150 K. While the qualitative visualization of natural luminosity and Schlieren images provides insight into the flame structure and reaction zones, a deeper understanding of spray combustion requires quantitative measurements. In this study, the effect of ambient properties, such as temperature, density and oxygen concentration, on ignition characteristics is evaluated through measurements of ignition delay and ignition distance, which are further discussed in the following section.

The influence of ambient density on ignition delay and ignition distance is illustrated in Figs. 3.12a–3.12b for 850 K, and in Figs. 3.13a–3.13b for 1150 K. Increasing the density from 14.38 to 27.24 kg/m^3 reduced ignition delay, restricted axial spray tip penetration due to stronger aerodynamic drag, and enhanced fuel–air mixing, resulting in a shorter and more compact flame structure. The effect of injection pressure is shown in Figs. 3.12a–3.13b.

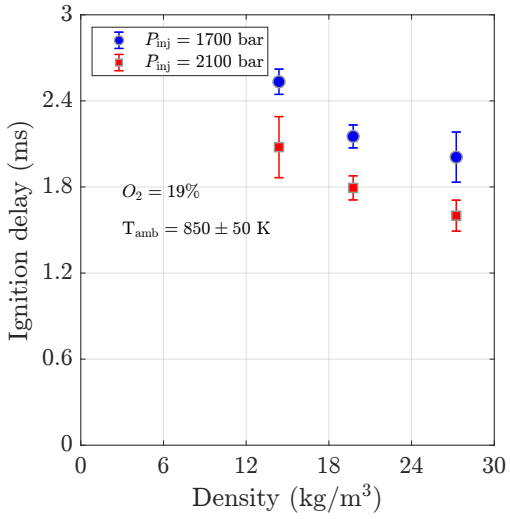

(a) Ignition delay versus density at 850 K.

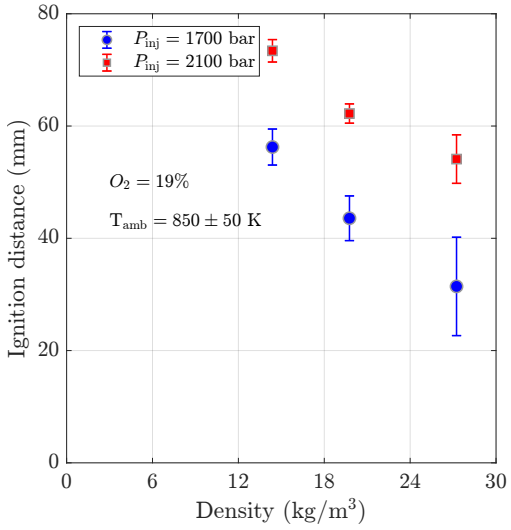

(b) Ignition distance versus density at 850 K.

Figure 3.12: Comparison of ignition delay and ignition distance at 850 K for varying ambient densities and injection pressures.

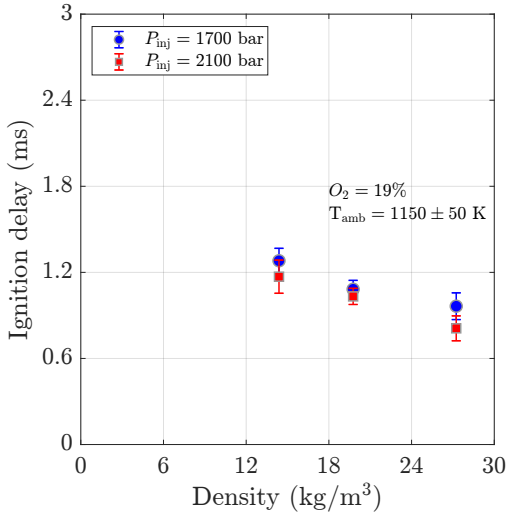

(a) Ignition delay versus density at 1150 K.

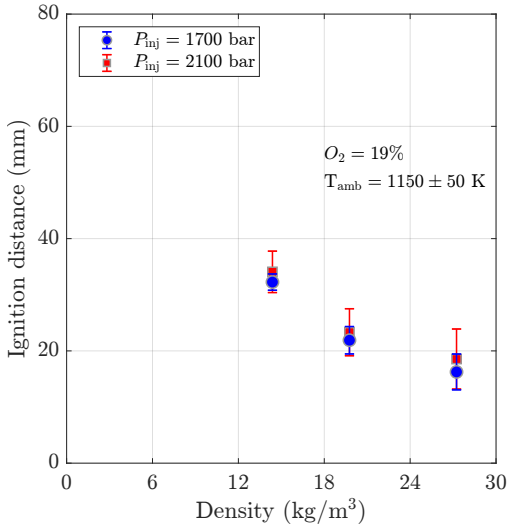

(b) Ignition distance versus density at 1150 K.

Figure 3.13: Comparison of ignition delay and ignition distance at 1150 K for varying ambient densities and injection pressures.

Raising the injection pressure to 2100 bar improved atomization, accelerated fuel–air mixing, and shortened ignition delay, whereas 1700 bar resulted in comparatively slower mixing and delayed ignition. Reduction of oxygen concentration from 19% to 13% further prolonged ignition delay and suppressed flame luminosity, particularly under low-temperature conditions. These results demonstrate that ignition delay, flame luminosity, and spray flame structure are governed by the combined effects of ambient density, temperature, injection pressure, and oxygen availability. The data illustrate the transition from premixed combustion at 850 K to diffusion-dominated combustion at 1150 K.

3.4 Results from near-field atomization

3.4.1 Summary of paper-E: Time-resolved ballistic imaging of transient Diesel spray

Ballistic imaging was used to study spray evolution under ambient back-pressure conditions at injection pressures of 1700 bar and 2100 bar. The analysis focused on three key spray characteristics within 10 mm of the nozzle: spray penetration length (Fig. 3.14a), spray cone angle (Fig. 3.14b), and spray area the spray. Penetration length was found to increase with injection pressure. At 2100 bar, the spray penetrates significantly further than at 1700 bar due to the higher injection momentum, allowing the fuel to travel longer distances. This increase in penetration is especially clear within the first few microseconds after the start of injection (ASOI), as shown in Fig. 3.14a. Similarly, the spray cone angle demonstrated a

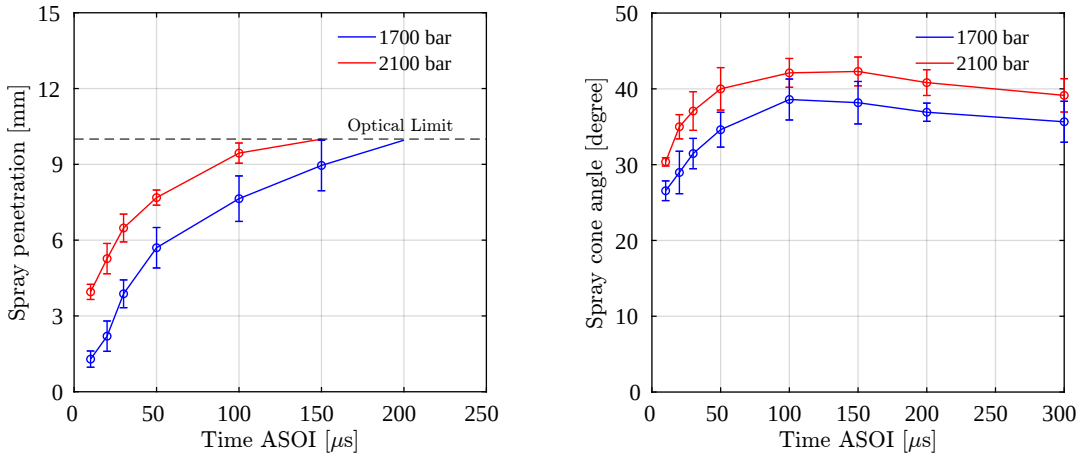

(a) Spray penetration length

(b) Spray cone angle

Figure 3.14: Spray characteristics at injection pressures $P_{\text{inj}} = 1700\,\text{bar}$ and $2100\,\text{bar}$, with ambient pressure $P_{\text{amb}} = 1\,\text{atm}$.

notable dependence on injection pressure during the transient near-field phase, which differs from earlier studies suggesting pressure insensitivity (X. Wang et al., 2010). The cone angle at 2100 bar was larger than at 1700 bar, mainly because the higher injection pressure

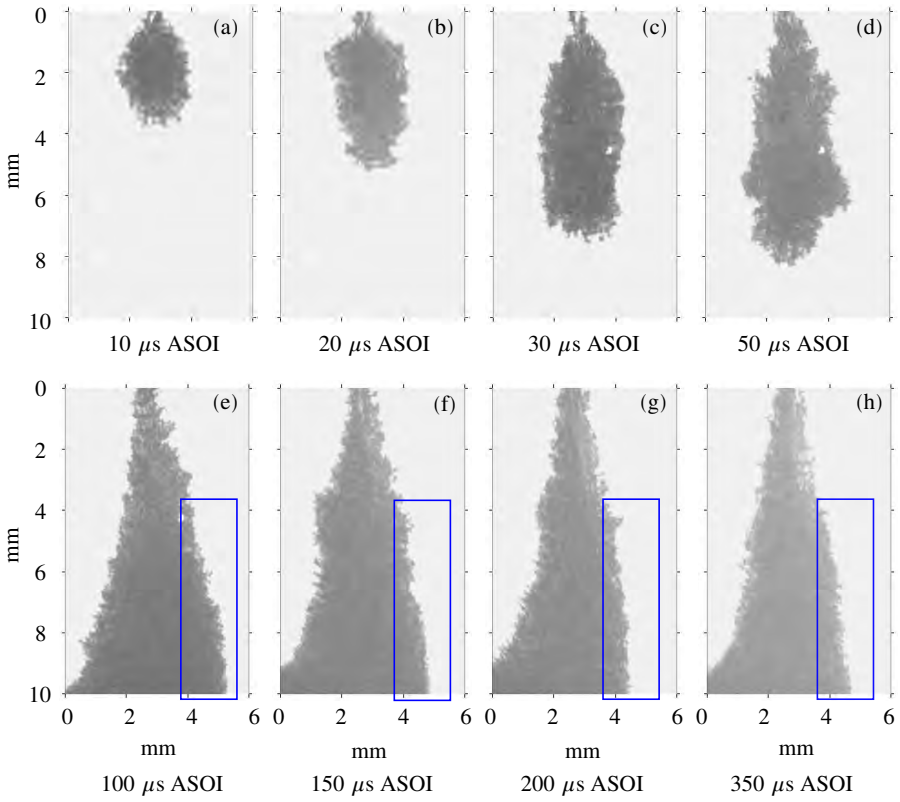

Figure 3.15: Spray evaluation at $P_{\mathrm{inj}} = 2100\,\mathrm{bar}$ and $P_{\mathrm{amb}} = 1\,\mathrm{atm}$.

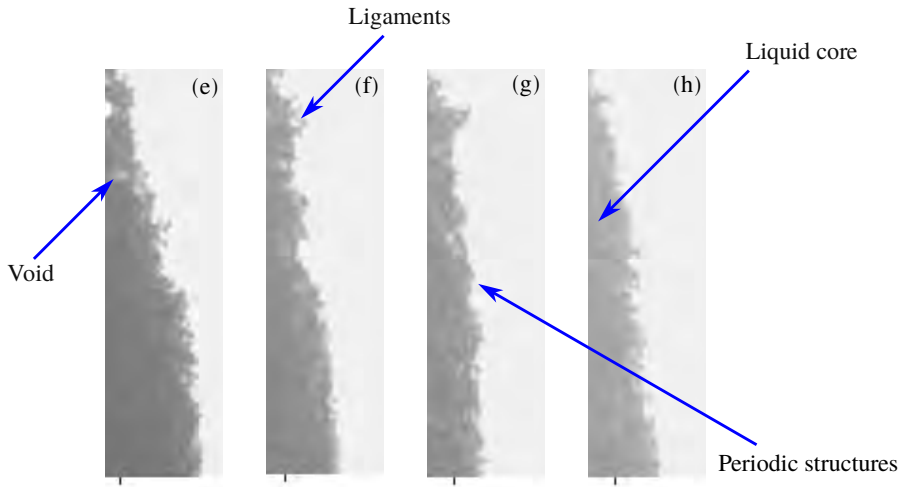

Figure 3.16: of spray edge structures from ballistic imaging at $P_{\mathrm{inj}} = 2100\,\mathrm{bar}$ and $P_{\mathrm{amb}} = 1\,\mathrm{atm}$.

imparts greater momentum to the spray, enhancing its lateral dispersion (Fig. 3.14b). This results in a distinct umbrella-shaped spray structure within the first 50 μs ASOI at 2100 bar (Fig. 3.15). Conversely, the lower momentum at 1700 bar produced a narrower cone angle with weaker interaction between the spray and ambient gas, reducing radial spreading. In addition, the spray area was observed to increase with injection pressure. The larger area at 2100 bar is attributed to both the deeper penetration and the wider cone angle, which allow the spray to spread more radially and cover a greater projected area within the image frame. The temporal evolution of spray morphology, captured in Fig. 3.15, further illustrates these differences. At 2100 bar, the early spray consists of a dense central core and an umbrella-shaped periphery, with ligament-like structures emerging from approximately 100 μs ASOI, signaling the onset of primary breakup. These ligaments persist throughout the injection event, captured, indicating sustained momentum and incomplete atomization as illustrated in Figs. 3.16(e–h). At 1700 bar, the spray morphology follows a similar pattern but with less pronounced umbrella structures and narrower cone angles. Ligaments and periodic surface features appear at the spray boundaries, but are weaker compared to the higher-pressure case. Additionally, localized voids and low-density regions, possibly caused by uneven atomization, are observed but occur less frequently than ligaments.

CHAPTER 4

Concluding Remarks and Future Work

4.1 Conclusions

This thesis has presented a comprehensive experimental investigation into the transient behavior of pilot fuel sprays from heavy-duty diesel injectors under conditions relevant to dual-fuel marine engine applications. Through the use of high-pressure, high-temperature optical spray test rigs and advanced imaging techniques, the study has addressed several critical knowledge gaps in the understanding of short-duration pilot injections. A plume isolation technique using a thimble-type structure was successfully developed and implemented, enabling the optical characterization of individual spray plumes from multi-hole injectors without interference from neighboring plumes. This approach allowed for detailed analysis of spray morphology, penetration, and ignition behavior under both non-reactive and reactive conditions. The study further explored plume-to-plume variations using Mie-scattering imaging, revealing insights into the consistency and symmetry of spray formation across different injector configurations. Single-plume experiments conducted under evaporative and reactive conditions provided valuable data on liquid and vapor phase behavior, ignition delay, and flame development. Additionally, time-resolved ballistic imaging was employed to investigate near-field spray atomization, capturing spray their evolution within a 10 mm radius within 10 mm of the nozzle. The influence of key operating parameters, such as fuel injection pressure under ambient gas density, was systematically studied, offering a deeper understanding of their effects on spray characteristics. Overall, the findings of this research contribute significantly to the fundamental understanding of pilot spray behavior in dual-fuel combustion systems. The insights gained are expected to support the

development of predictive combustion models and the optimization of injection strategies for efficient dual-fuel engine operation.

4.2 Future work

While this study has provided valuable insights, several areas remain open for further exploration:

- Investigate the influence of different injector geometries, such as nozzle hole diameter, length-to-diameter ratio, and sac volume, on spray atomization and ignition characteristics under short-duration injection conditions.
- Study the interaction between pilot and main injections, particularly in split injection strategies, to understand their impact on ignition stability and emissions in dual-fuel engines.
- Investigate the velocity and acceleration vectors of the spray using ballistic imaging.
- Use two-photon laser-induced fluorescence (2p-LIF) laser sheet imaging to analyze the structure and atomization behavior of fuel sprays.
- Implement optical sectioning techniques to obtain high-resolution, plane-specific measurements within transient sprays for accurate characterization of liquid and vapor phase dynamics.

References

Agarwal, Avinash Kumar et al., eds. (2022). *Advanced Combustion for Sustainable Transport*. Energy, Environment, and Sustainability. Singapore: Springer Singapore. ISBN: 978-981-16-8417-3 978-981-16-8418-0. DOI: 10.1007/978-981-16-8418-0. URL: https://link.springer.com/10.1007/978-981-16-8418-0.

Arai, M. et al. (Feb. 1984). "Disintegrating Process and Spray Characterization of Fuel Jet Injected by a Diesel Nozzle". In: *SAE International Congress and Exposition*. SAE International. DOI: https://doi.org/10.4271/840275. URL: https://doi.org/10.4271/840275.

Ashgriz, Nasser, ed. (2011). *Handbook of Atomization and Sprays: Theory and Applications*. Boston, MA: Springer US. ISBN: 978-1-4419-7263-7 978-1-4419-7264-4. DOI: 10.1007/978-1-4419-7264-4. URL: https://link.springer.com/10.1007/978-1-4419-7264-4.

Baert, Rik S.G. et al. (2009). "Design and operation of a high pressure, high temperature cell for HD diesel spray diagnostics: Guidelines and results". In: DOI: 10.4271/2009-01-0649.

Bardi, Michele et al. (2012). "Engine combustion network: comparison of spray development, vaporization, and combustion in different combustion vessels". In: *Atomization and Sprays* 22.10, pp. 807–842. ISSN: 1044-5110. DOI: 10.1615/AtomizSpr.2013005837. URL: http://www.dl.begellhouse.com/journals/6a7c7e10642258cc,5b18f0e860ebc687,20adc8ff175d5f43.html.

Canaan, Robert E. et al. (1998). "The Influence of Fuel Volatility on the Liquid-Phase Fuel Penetration in a Heavy-Duty D.I. Diesel Engine". In:

SAE Transactions 107, pp. 583–602. ISSN: 0096736X, 25771531. URL: http://www.jstor.org/stable/44736554.

Chandra, R et al. (Nov. 2011). "Performance evaluation of a constant speed IC engine on CNG, methane enriched biogas and biogas". In: *Applied Energy* 88 (11), pp. 3969–3977. ISSN: 03062619. DOI: 10.1016/j.apenergy.2011.04.032. URL: https://linkinghub.elsevier.com/retrieve/pii/S0306261911002546.

Delacourt, E, B Desmet, and B Besson (May 2005). "Characterisation of very high pressure diesel sprays using digital imaging techniques". In: *Fuel* 84 (7-8), pp. 859–867. ISSN: 00162361. DOI: 10.1016/j.fuel.2004.12.003. URL: https://linkinghub.elsevier.com/retrieve/pii/S0016236105000062.

Desantes, J. M. et al. (2005). "Experimental characterization of internal nozzle flow and diesel spray behavior. part II: Evaporative conditions". In: *Atomization and Sprays* 15.5, pp. 517–544. DOI: 10.1615/atomizspr.v15.i5.30.

Deshmukh, Devendra (2011). "Studies on Atomization and Sprays of Plant Oil Biofuels Using Laser-Based Diagnostics". PhD thesis. PhD thesis. Bangalore, India: Indian Institute of Science.

Dong, PengBo et al. (Apr. 2016). "Characterization of Internal Flow and Spray Behaviors of Hole-Type Nozzle under Tiny and Normal Injection Quantity Conditions for Diesel Engine". In: *SAE International Journal of Fuels and Lubricants* 9 (1), pp. 125–137. ISSN: 1946-3960. DOI: 10.4271/2016-01-0862. URL: https://www.sae.org/content/2016-01-0862/.

Du, Wei et al. (2017). "Effects of injection pressure on diesel sprays in constant injection mass condition". In: *Applied Thermal Engineering* 121, pp. 234–241. ISSN: 1359-4311. DOI: https://doi.org/10.1016/j.applthermaleng.2017.04.075. URL: https://www.sciencedirect.com/science/article/pii/S1359431116340686.

Emberson, D R et al. (May 2016). "Optical characterization of Diesel and water emulsion fuel injection sprays using shadowgraphy". In: *Fuel* 172, pp. 253–262. ISSN: 00162361. DOI: 10.1016/j.fuel.2016.01.015. URL: https://linkinghub.elsevier.com/retrieve/pii/S0016236116000247.

Espey, Christoph and John E. Dec (Oct. 1, 1995). "The Effect of TDC Temperature and Density on the Liquid-Phase Fuel Penetration in a D. I. Diesel Engine". In: 1995 SAE International Fall Fuels and Lubricants Meeting and

Exhibition, p. 952456. DOI: 10.4271/952456. URL: https://www.sae.org/content/952456/.

Farrell, P V, C T Chang, and T F Su (Feb. 1996). "High Pressure Multiple Injection Spray Characteristics". In: p. 960860. DOI: 10.4271/960860. URL: https://www.sae.org/content/960860/.

Frühhaber, Jens et al. (Sept. 2018). "Modeling the Pilot Injection and the Ignition Process of a Dual Fuel Injector with Experimental Data from a Combustion Chamber Using Detailed Reaction Kinetics". In: *International Powertrains, Fuels & Lubricants Meeting*. SAE International. URL: https://www.sae.org/publications/technical-papers/content/2018-01-1724/.

Gimeno, Jaime et al. (2016). "Experimental study of the injection conditions influence over n-dodecane and diesel sprays with two ECN single-hole nozzles. Part I: Inert atmosphere". In: *Energy Conversion and Management* 126, pp. 1146–1156. ISSN: 0196-8904. DOI: https://doi.org/10.1016/j.enconman.2016.07.077. URL: https://www.sciencedirect.com/science/article/pii/S0196890416306562.

Gonzalez, Rafael C (2009). *Digital image processing*. Pearson education india.

Hiroyasu, Hiro and Masataka Arai (Feb. 1990). "Structures of Fuel Sprays in Diesel Engines". en. In: p. 900475. DOI: 10.4271/900475. URL: https://www.sae.org/content/900475/.

International Maritime Organization (2020). *Tier III NOx Emission Standards*. https://www.imo.org/en/OurWork/Environment/Pages/Tier-III.aspx.

Ju, Dehao et al. (Oct. 2014). "Quantitative Comparisons of Macroscopic Characteristics of a Flash-Boiling Spray and a Turbulent Round Jet". en. In: pp. 2014–01–2748. DOI: 10.4271/2014-01-2748. URL: https://www.sae.org/content/2014-01-2748/.

Ju, Yiguang (2021). "Understanding cool flames and warm flames". In: *Proceedings of the Combustion Institute* 38.1, pp. 83–119. ISSN: 1540-7489. DOI: https://doi.org/10.1016/j.proci.2020.09.019. URL: https://www.sciencedirect.com/science/article/pii/S1540748920306805.

Jung, Yongjin et al. (Apr. 2015). "Measurement of Liquid and Vapor Penetration of Diesel Sprays with a Variation in Spreading Angle". In: *SAE 2015 World Congress & Exhibition*. SAE International. DOI: https://doi.org/10.4271/2015-01-0946. URL: https://doi.org/10.4271/2015-01-0946.

Karatuğ, Çağlar et al. (Dec. 2023). "Environmental and Economic Evaluation of Dual-Fuel Engine Investment of a Container Ship". In: *Journal of Marine Science and Application* 22.4, pp. 823–836. ISSN: 1671-9433, 1993-5048. DOI: 10.1007/s11804-023-00381-3. URL: https://link.springer.com/10.1007/s11804-023-00381-3.

Kim, Kihyun et al. (2013). "Spray and combustion characteristics of gasoline and diesel in a direct injection compression ignition engine". In: *Fuel* 109, pp. 616–626. ISSN: 0016-2361. DOI: https://doi.org/10.1016/j.fuel.2013.02.060. URL: https://www.sciencedirect.com/science/article/pii/S0016236113001622.

Kook, Sanghoon and Lyle M Pickett (2012). "Liquid length and vapor penetration of conventional, Fischer–Tropsch, coal-derived, and surrogate fuel sprays at high-temperature and high-pressure ambient conditions". In: *Fuel* 93, pp. 539–548. DOI: https://doi.org/10.1016/j.fuel.2011.10.004. URL: https://www.sciencedirect.com/science/article/abs/pii/S0016236111006211.

Lazaroiu, George Cristian, Mariacristina Roscia, and Vasile Sebastian Dancu, eds. (2024). *Energy Transition Holistic Impact Challenge (ETHIC): A New Environmental and Climatic Era*. en. Environmental Science and Engineering. Cham: Springer Nature Switzerland. ISBN: 978-3-031-55447-6 978-3-031-55448-3. DOI: 10.1007/978-3-031-55448-3. URL: https://link.springer.com/10.1007/978-3-031-55448-3.

Lazaroiu, Gheorghe and Lucian Mihaescu, eds. (2021). *Innovative Renewable Waste Conversion Technologies*. en. Cham: Springer International Publishing. ISBN: 978-3-030-81430-4 978-3-030-81431-1. DOI: \url{10.1007/978-3-030-81431-1}. URL: %5Curl%7Bhttps://link.springer.com/10.1007/978-3-030-81431-1%7D.

Lefebvre, Arthur H. and Vincent G. McDonell (2017). *Atomization and sprays*. Second edition. Combustion: an international series. Boca Raton London New York: CRC Press, Taylor & Francis Group. 1 p. ISBN: 978-1-4987-3625-1 978-1-315-12091-1 978-1-4987-3626-8 978-1-351-63773-2. DOI: 10.1201/9781315120911.

Linne, Mark et al. (June 2006). "Ballistic imaging of the near field in a diesel spray". In: *Experiments in Fluids* 40.6. ISSN: 0723-4864, 1432-1114. DOI: 10.1007/s00348-006-0122-0. URL: http://link.springer.com/10.1007/s00348-006-0122-0.

Linne, Mark A. et al. (2009). "Ballistic imaging of liquid breakup processes in dense sprays". In: *Proceedings of the Combustion Institute* 32.2, pp. 2147–2161. ISSN: 1540-7489. DOI: https://doi.org/10.1016/j.proci.2008.07.040. URL: https://www.sciencedirect.com/science/article/pii/S1540748908000308.

Lokesh, M (Nov. 2017). "Studies on Droplet-Droplet Collisions". Submitted in partial fulfillment of the requirements for the degree of Master of Science (by Research). Master of Science (by Research) thesis. Chennai, India: Department of Mechanical Engineering, Indian Institute of Technology Madras.

Macian, V et al. (Nov. 2012). "Experimental Evaluation of the Best Approach for Diesel Spray Images Segmentation". In: *Experimental Techniques* 36 (6), pp. 26–34. ISSN: 07328818. DOI: 10.1111/j.1747-1567.2011.00730.x. URL: http://doi.wiley.com/10.1111/j.1747-1567.2011.00730.x.

Meijer, Maarten et al. (2013). "High-Speed Characterization of ECN Spray A Using Various Diagnostic Techniques". In: *SAE International Journal of Engines* 6.2, pp. 1238–1248. ISSN: 19463936, 19463944. URL: http://www.jstor.org/stable/26277697.

Mittal, Mayank et al. (June 2011). "Fuel spray visualization and its impingement analysis on in-cylinder surfaces in a direct-injection spark-ignition engine". In: *Journal of Visualization* 14.2, pp. 149–160. ISSN: 1343-8875, 1875-8975. DOI: 10.1007/s12650-011-0083-0. URL: http://link.springer.com/10.1007/s12650-011-0083-0.

Mohandas, Anu, Hongrong Luo, and Seeram Ramakrishna (2021). "An Overview on Atomization and Its Drug Delivery and Biomedical Applications". In: *Applied Sciences* 11.11. ISSN: 2076-3417. DOI: 10.3390/app11115173. URL: https://www.mdpi.com/2076-3417/11/11/5173.

Moreira, A.L.N., A.S. Moita, and M.R. Panão (2010). "Advances and challenges in explaining fuel spray impingement: How much of single droplet impact research is useful?" In: *Progress in Energy and Combustion Science* 36.5, pp. 554–580. ISSN: 0360-1285. DOI: https://doi.org/10.1016/j.pecs.2010.01.002. URL: https://www.sciencedirect.com/science/article/pii/S0360128510000031.

Musculus, Mark P.B., Paul C. Miles, and Lyle M. Pickett (2013). "Conceptual models for partially premixed low-temperature diesel combustion". In: *Progress in Energy and Combustion Science* 39.2, pp. 246–283. ISSN: 0360-

1285. DOI: https://doi.org/10.1016/j.pecs.2012.09.001. URL: https://www.sciencedirect.com/science/article/pii/S0360128512000548.

Naber, Jeffrey and Dennis L Siebers (Feb. 1996). "Effects of Gas Density and Vaporization on Penetration and Dispersion of Diesel Sprays". In: p. 960034. DOI: 10.4271/960034. URL: https://www.sae.org/content/960034/.

Ohnesorge, Wolfgang V (1936). "Die bildung von tropfen an düsen und die auflösung flüssiger strahlen". In: *ZAMM-Journal of Applied Mathematics and Mechanics/Zeitschrift für Angewandte Mathematik und Mechanik* 16.6, pp. 355–358.

Okajima, S and S Kumagai (Jan. 1991). "Experimental investigation of soot and NOx reduction by impinging spray combustion in a closed vessel". In: *Symposium (International) on Combustion* 23 (1), pp. 275–279. ISSN: 00820784. DOI: 10.1016/S0082-0784(06)80270-5. URL: https://linkinghub.elsevier.com/retrieve/pii/S0082078406802705.

Okubo, Masaaki and Takuya Kuwahara (2020). "Chapter 5 - Prospects for marine diesel engine emission control". In: *New Technologies for Emission Control in Marine Diesel Engines*. Ed. by Masaaki Okubo and Takuya Kuwahara. Butterworth-Heinemann, pp. 211–266. ISBN: 978-0-12-812307-2. DOI: https://doi.org/10.1016/B978-0-12-812307-2.00005-5. URL: https://www.sciencedirect.com/science/article/pii/B9780128123072000055.

Ong, Jiun Cai et al. (2021). "Effects of ambient pressure and nozzle diameter on ignition characteristics in diesel spray combustion". In: *Fuel* 290, p. 119887. ISSN: 0016-2361. DOI: https://doi.org/10.1016/j.fuel.2020.119887. URL: https://www.sciencedirect.com/science/article/pii/S0016236120328830.

Otsu, Nobuyuki (1979). "A Threshold Selection Method from Gray-Level Histograms". In: *IEEE Transactions on Systems, Man, and Cybernetics* 9.1, pp. 62–66. DOI: 10.1109/TSMC.1979.4310076.

Pal, Manas Kumar (2019). "Effect of ambient fuel vapour concentration on the liquid length and air-fuel mixing of an evaporating spray". In: *Fuel* 256, p. 115945. ISSN: 0016-2361. DOI: https://doi.org/10.1016/j.fuel.2019.115945. URL: https://www.sciencedirect.com/science/article/pii/S0016236119312979.

Pal, Manas Kumar and Shamit Bakshi (2017). "Study of the effect of ambient vapour concentration on the spray structure of an evaporating n-hexane

spray". In: *Experimental Thermal and Fluid Science* 88, pp. 566–575. ISSN: 0894-1777. DOI: https://doi.org/10.1016/j.expthermflusci.2017.07.013. URL: https://www.sciencedirect.com/science/article/pii/S0894177717302091.

Pastor, José V et al. (Feb. 2007). "Segmentation of diesel spray images with log-likelihood ratio test algorithm for non-Gaussian distributions". In: *Applied Optics* 46 (6), p. 888. ISSN: 0003-6935, 1539-4522. DOI: 10.1364/AO.46.000888. URL: https://opg.optica.org/abstract.cfm?URI=ao-46-6-888.

Payri, F et al. (2014). "Engine combustion network: Influence of the gas properties on the spray penetration and spreading angle". In: *Experimental Thermal and Fluid Science* 53, pp. 236–243.

Payri, R et al. (Apr. 2008). "Macroscopic Behavior of Diesel Sprays in the Near-Nozzle Field". In: *SAE International Journal of Engines* 1 (1), pp. 528–536. ISSN: 1946-3944. DOI: 10.4271/2008-01-0929. URL: https://www.sae.org/content/2008-01-0929/.

Payri, R., J. Gimeno, et al. (Aug. 2016). "Study of liquid and vapor phase behavior on Diesel sprays for heavy duty engine nozzles". In: *Applied Thermal Engineering* 107, pp. 365–378. ISSN: 1359-4311. DOI: 10.1016/J.APPLTHERMALENG.2016.06.159.

Payri, R., F.J. Salvador, et al. (2011). "Flow regime effects on non-cavitating injection nozzles over spray behavior". In: *International Journal of Heat and Fluid Flow* 32.1, pp. 273–284. ISSN: 0142-727X. DOI: https://doi.org/10.1016/j.ijheatfluidflow.2010.10.001. URL: https://www.sciencedirect.com/science/article/pii/S0142727X10001633.

Payri, Raul, Jose M. García-Oliver, et al. (2012). "Fuel temperature influence on diesel sprays in inert and reacting conditions". In: *Applied Thermal Engineering* 35, pp. 185–195. ISSN: 1359-4311. DOI: https://doi.org/10.1016/j.applthermaleng.2011.10.027. URL: https://www.sciencedirect.com/science/article/pii/S1359431111005655.

Payri, Raul, Jaime Gimeno, Joaquin De la Morena, et al. (2016). "Study of new prototype pintle injectors for diesel engine application". In: *Energy Conversion and Management* 122, pp. 419–427. ISSN: 0196-8904. DOI: https://doi.org/10.1016/j.enconman.2016.06.003. URL: https://www.sciencedirect.com/science/article/pii/S0196890416304824.

Payri, Raul, Jaime Gimeno, Juan P Viera, et al. (Nov. 2013). "Needle lift profile influence on the vapor phase penetration for a prototype diesel direct acting piezoelectric injector". In: *Fuel* 113, pp. 257–265. ISSN: 00162361. DOI: 10.1016/j.fuel.2013.05.057. URL: https://linkinghub.elsevier.com/retrieve/pii/S0016236113004699.

Payri, Raul, F. Javier Salvador, et al. (2020). "Study of evaporative diesel spray interaction in multiple injections using optical diagnostics". In: *Applied Thermal Engineering* 176, p. 115402. ISSN: 1359-4311. DOI: https://doi.org/10.1016/j.applthermaleng.2020.115402. URL: https://www.sciencedirect.com/science/article/pii/S1359431120311649.

Payri, Raul, F.J. Salvador, et al. (Oct. 2015). "Experimental Analysis on the Influence of Nozzle Geometry Over the Dispersion of Liquid N-Dodecane Sprays". In: *Frontiers in Mechanical Engineering* 1. DOI: 10.3389/fmech.2015.00013.

Payri, Raul, Juan P. Viera, et al. (2017). "The effect of nozzle geometry over the evaporative spray formation for three different fuels". In: *Fuel* 188, pp. 645–660. ISSN: 0016-2361. DOI: https://doi.org/10.1016/j.fuel.2016.10.064. URL: https://www.sciencedirect.com/science/article/pii/S0016236116310262.

Pereda, Paula Carvalho et al. (2025). "Sustainable Shipping: Modeling Economic and Greenhouse Gas Impacts of Decarbonization Policies (Part II)". In: *Sustainability* 17.9. ISSN: 2071-1050. DOI: 10.3390/su17093765. URL: https://www.mdpi.com/2071-1050/17/9/3765.

Phan, Anthony (Jan. 2009). "Development of a Rate of Injection Bench and Constant Volume Combustion Chamber for Diesel Spray Diagnostics". Master's thesis. MA thesis. Ames, Iowa, USA: Iowa State University. URL: https://dr.lib.iastate.edu/handle/20.500.12876/24897.

Pickett, Lyle M et al. (2010). "Comparison of diesel spray combustion in different high-temperature, high-pressure facilities". In: *SAE International Journal of Engines* 3.2, pp. 156–181.

Pickett, Lyle M., Sanghoon Kook, and Timothy C. Williams (Apr. 20, 2009). "Visualization of Diesel Spray Penetration, Cool-Flame, Ignition, High-Temperature Combustion, and Soot Formation Using High-Speed Imaging". In: *SAE International Journal of Engines* 2.1, pp. 439–459. ISSN: 1946-3944. DOI: 10.4271/2009-01-0658. URL: https://www.sae.org/content/2009-01-0658/.

Pounder, C Coulson and D F Woodyard (2004). *Pounder's marine diesel engines and gas turbines*. 8th ed. OCLC: ocm53231381. Elsevier Butterworth Heinemann. ISBN: 978-0-7506-5846-1.

Rayleigh, Lord (Nov. 1878). "On The Instability Of Jets". In: *Proceedings of the London Mathematical Society* s1-10.1, pp. 4–13. ISSN: 0024-6115. DOI: 10.1112/plms/s1-10.1.4. eprint: https://academic.oup.com/plms/article-pdf/s1-10/1/4/4334010/s1-10-1-4.pdf. URL: https://doi.org/10.1112/plms/s1-10.1.4.

Reitz, Rolf D. (1978). "ATOMIZATION AND OTHER BREAKUP REGIMES OF A LIQUID JET". English. Copyright - Database copyright ProQuest LLC; ProQuest does not claim copyright in the individual underlying works; Last updated - 2023-02-18. PhD thesis, p. 336. ISBN: 9798661024862. URL: http://proxy.lib.chalmers.se/login?url=https://www.proquest.com/dissertations-theses/atomization-other-breakup-regimes-liquid-jet/docview/302918755/se-2.

Rubio-Gómez, Guillermo et al. (May 2018). "Automatic macroscopic characterization of diesel sprays by means of a new image processing algorithm". In: *Measurement Science and Technology* 29 (5), p. 55406. ISSN: 0957-0233, 1361-6501. DOI: 10.1088/1361-6501/aab121. URL: https://iopscience.iop.org/article/10.1088/1361-6501/aab121.

Ruiz-Rodriguez, Irene et al. (2019). "Investigation of Spray Angle Measurement Techniques". In: *IEEE Access* 7, pp. 22276–22289. ISSN: 2169-3536. DOI: 10.1109/ACCESS.2019.2899214. URL: https://ieeexplore.ieee.org/document/8641265/.

Sedarsky, David, Mattias Rahm, and Mark Linne (Apr. 2016). "Visualization of acceleration in multiphase fluid interactions". In: *Opt. Lett.* 41.7, pp. 1404–1407. DOI: 10.1364/OL.41.001404. URL: https://opg.optica.org/ol/abstract.cfm?URI=ol-41-7-1404.

Senecal, P. K. et al. (Mar. 2003). "Multi-Dimensional Modeling of Direct-Injection Diesel Spray Liquid Length and Flame Lift-off Length using CFD and Parallel Detailed Chemistry". In: *SAE 2003 World Congress & Exhibition*. SAE International. DOI: https://doi.org/10.4271/2003-01-1043. URL: https://doi.org/10.4271/2003-01-1043.

Settles, Gary S (2001). *Schlieren and shadowgraph techniques: visualizing phenomena in transparent media*. Springer Science & Business Media.

Shao, J et al. (July 2003). "Quantitative characterization of diesel sprays using digital imaging techniques". In: *Measurement Science and Technology* 14 (7), pp. 1110–1116. ISSN: 0957-0233, 1361-6501. DOI: 10.1088/0957-0233/14/7/328. URL: https://iopscience.iop.org/article/10.1088/0957-0233/14/7/328.

Siebers, Dennis L. (Feb. 1998). "Liquid-Phase Fuel Penetration in Diesel Sprays". In: *International Congress & Exposition*. SAE International. DOI: https://doi.org/10.4271/980809. URL: https://doi.org/10.4271/980809.

Sombatwong, Pisarn, Prachasanti Thaiyasuit, and Kulachate Pianthong (2013). "Effect of Pilot Fuel Quantity on the Performance and Emission of a Dual Producer Gas–Diesel Engine". In: *Energy Procedia* 34, pp. 218–227. ISSN: 18766102. DOI: 10.1016/j.egypro.2013.06.750. URL: https://linkinghub.elsevier.com/retrieve/pii/S1876610213009934.

Suraj, C K et al. (June 2021). "Effects of autooxidation on the fuel spray characteristics of Karanja biodiesel". In: *Biomass and Bioenergy* 149, p. 106084. ISSN: 09619534. DOI: 10.1016/j.biombioe.2021.106084. URL: https://linkinghub.elsevier.com/retrieve/pii/S0961953421001215.

United Nations Conference on Trade and Development (UNCTAD) (2013). *Review of Maritime Transport 2013*. https://unctad.org/news/world-seaborne-trade-grew-just-38-2013-new-report-reveals. New York and Geneva.

Wang, Dongfang et al. (2023). "Experimental investigation of transition process from LTC to ITC and HTC during diesel spray combustion at low ambient temperatures". In: *Fuel* 333, p. 126372. ISSN: 0016-2361. DOI: https://doi.org/10.1016/j.fuel.2022.126372. URL: https://www.sciencedirect.com/science/article/pii/S0016236122031969.

Wang, Xiangang et al. (2010). "Experimental and analytical study on biodiesel and diesel spray characteristics under ultra-high injection pressure". In: *International Journal of Heat and Fluid Flow* 31.4, pp. 659–666. ISSN: 0142-727X. DOI: https://doi.org/10.1016/j.ijheatfluidflow.2010.03.006. URL: https://www.sciencedirect.com/science/article/pii/S0142727X1000069X.

Wärtsilä (2025). *Marine Dual Fuel Engines*. https://www.wartsila.com/marine/products/engines-and-generating-sets/dual-fuel-engines.

Wärtsilä Corporation (2023). *Wärtsilä: Innovative Technologies and Lifecycle Solutions*. URL: https://www.wartsila.com.

Weber, C (1939). "Disintegration of liquid jets". In: *Z. Angew. Math. Mech.* 11, pp. 135–159.

Xie, Hongzhan et al. (2015). "An Experimental Study on the Macroscopic Spray Characteristics of Biodiesel and Diesel in a Constant Volume Chamber". In: *Energies* 8.6, pp. 5952–5972. ISSN: 1996-1073. DOI: 10.3390/en8065952. URL: https://www.mdpi.com/1996-1073/8/6/5952.

Zheng, Liang et al. (Jan. 2015). "An optical study on liquid-phase penetration, flame lift-off location and soot volume fraction distribution of gasoline–diesel blends in a constant volume vessel". In: *Fuel* 139, pp. 365–373. ISSN: 00162361. DOI: 10.1016/j.fuel.2014.09.009. URL: https://linkinghub.elsevier.com/retrieve/pii/S0016236114008692.